

Bromine speciation and partitioning in slab-derived aqueous fluids and silicate melts and implications for halogen transfer in subduction zones

Marion Louvel^{1,2}, Carmen Sanchez-Valle², Wim J. Malfait³, Gleb S. Pokrovski⁴, Camelia N. Borca⁵ and Daniel Grolimund⁵

¹School of Earth Sciences, Bristol University, UK- BS81RJ, Bristol, United-Kingdom

²Institute for Mineralogy, WW-Universität Münster, D-48149, Münster, Germany

³Swiss Federal Laboratories for Materials Science and Technology EMPA, CH-8600, Dübendorf, Switzerland

⁴Groupe Métallogénie Expérimentale, Géosciences Environnement Toulouse (GET - UMR 5563), OMP-CNRS-IRD-University of Toulouse III Paul Sabatier, 31400 Toulouse, France

⁵Swiss Light Source, Paul Scherrer Institute, CH-5232, Villigen, Switzerland

Correspondence to: Marion Louvel (louvel@uni-muenster.de)

Abstract. Understanding the behavior of halogens (Cl, Br, and I) in subduction zones is critical to constrain the geochemical cycle of these volatiles and associated trace metals, and to quantify the halogen fluxes to the atmosphere *via* volcanic degassing. Here, the partitioning of bromine between coexisting aqueous fluids and hydrous granitic melts and its speciation in slab-derived fluids have been investigated *in situ* up to 840 °C and 2.2 GPa by synchrotron X-ray fluorescence (SXRF) and x-ray absorption spectroscopy (XAS) in diamond-anvil cells. The partition coefficients $D_{\text{Br}}^{\text{fm}}$ range from ~2 to ~15, with an average value of 6.7 ± 3.6 (1σ) over the whole pressure-temperature (*P-T*) range, indicating a moderate Br enrichment in aqueous fluids, in agreement with previous work. EXAFS analysis further evidences a gradual evolution of Br speciation from hydrated Br ions $[\text{Br}(\text{H}_2\text{O})_6]$ in slab dehydration fluids to more complex structures involving both Na ions and water molecules, $[\text{BrNa}_x(\text{H}_2\text{O})_y]$, in hydrous silicate melts and supercritical fluids released at greater depth (> 200 km). In denser fluids ($\rho > 1.5 \text{ g.cm}^{-3}$), containing 60 wt% dissolved alkali-silicates and in hydrous $\text{Na}_2\text{Si}_2\text{O}_5$ melts (10 wt% H_2O), Br is found to be in a “salt-like” structure involving 6 nearest Na ions and several next-nearest O neighbors that are either from water molecules and/or the silicate network. Bromine (and likely chlorine and iodine) complexing with alkalis is thus an efficient mechanism for the mobilization and transport of halogens by hydrous silicate melts and silica-rich supercritical fluids. Our results suggest that both shallow dehydration fluids and deeper silicate-bearing fluids efficiently remove halogens from the slab in the sub-arc region, thus favoring an efficient transfer of halogens across subduction zones.

Keywords: Halogen cycle, speciation, partitioning, slab-derived fluid, subduction zone, silicate melt, diamond anvil cell.

35 **1 Introduction**

36 The fluxes of volatile elements (water, carbon, sulfur, and halogens) in subduction zones
37 play a critical role in the Earth's chemical evolution; however, the mechanisms and extent of their
38 transfer from slab components to the mantle wedge, the volcanic arc and, ultimately, the
39 atmosphere remain poorly understood. Although halogens (F, Cl, Br and I) are rather minor
40 volatiles compared to H₂O and CO₂, their effect on the physical and chemical properties of slab-
41 derived fluids and arc magmas (*e.g.* phase equilibria, viscosity, density), as well as their ability to
42 bind to trace elements and base metals (*e.g.*, Au, Cu, Zn, Pb, REE) makes them key players in
43 the chemical transfer in subduction zones and formation of ore deposits (*e.g.*, Zellmer et al.,
44 2015; Barnes et al., 2018). Furthermore, their emission to the troposphere and stratosphere at
45 volcanic arc centres may have a significant environmental impact, including ozone depletion by
46 Br (Bobrowski et al., 2003; von Glasow et al., 2009; Kutterolf et al., 2013). Constraining the
47 halogen cycle in subduction zones is thus crucial for assessing their impact on the global
48 atmospheric chemistry and climate.

49 In the last decade, new developments in quantification techniques on pore fluids, fluid
50 inclusions and rocks as well as in detection methods for halogens species in volcanic gases
51 enabled better estimates of halogen fluxes in subduction zones (Wallace, 2005; Pyle and Mather
52 2009; John et al., 2011; Kendrick et al., 2013; Kendrick et al., 2015; Chavrit et al., 2016; Barnes
53 et al., 2018). For example, comparisons of the input from the subducted sediments, altered
54 oceanic crust and serpentized oceanic lithosphere to the output along volcanic arcs point to a
55 significant imbalance between fluorine input and output, suggesting that a significant amount of
56 F may be transferred to the deep mantle (Roberge et al., 2015; Grutzner et al., 2017). On the
57 contrary, Cl, Br and I appear to be efficiently recycled up to the surface, either through shallow

58 loss of fluids to the fore-arc region (Br and especially I) or deeper release upon slab dehydration
59 (especially Cl and Br, and to a lesser extent I) (Kendrick et al., 2018). Yet, the poor
60 understanding of the transfer mechanisms and pathways of halogens limits the development of
61 numerical models constraining the role of fluids in the global cycling of elements in subduction
62 zones (Ikemoto and Iwamori, 2014; Kimura et al., 2016). There is for instance virtually no
63 constraint on the amounts of residual halogens that may be stored in the dehydrated slab or lost
64 to the continental crust through hidden hydrothermal activity and passive degassing. Similarly,
65 current knowledge of halogens solubility and speciation in fluids and melts is mostly limited to
66 pressures below 0.3 GPa (equivalent to ~10 km depth), which are relevant to volcanic degassing
67 and ore deposit formation in the shallow crust (Webster, 1990; Métrich and Rutherford, 1992;
68 Webster, 1992; Bureau et al., 2000; Signorelli and Carroll, 2002; Bureau and Métrich, 2003;
69 Carroll, 2005; Evans et al., 2009; Cadoux et al., 2018), but not to slab dehydration or melting
70 beneath arcs at far greater depth. Only recently, Bureau et al. (2010, 2016) reported fluid-melt
71 partition coefficients for Br and I in the haplogranite-H₂O system up to 1.7 GPa while Cochain et
72 al. (2015) investigated the speciation of Br in haplogranitic melts up to 7.6 GPa. Nevertheless,
73 the effect of fluid chemistry on the speciation and partitioning of halogens at high pressures and
74 temperatures (*P-T*) remains unknown in subduction zones. To fill this gap, we combined
75 synchrotron X-ray fluorescence (SXRF) and X-ray absorption spectroscopy (XAS)
76 measurements in a hydrothermal diamond-anvil cell (HDAC) to investigate Br fluid-melt
77 partitioning and speciation in aqueous fluids and hydrous silicate melts that mimic the mobile
78 phases released by the slab at sub-arc depths (Manning, 2004; Frezzotti and Ferrando, 2015).
79 Bromine is employed here as an analog of chlorine amenable to SXRF and XAS studies through
80 the diamond window of the HDAC due to its higher absorption edge energy (13.47 keV for

81 bromine K-edge compared to 2.82 keV for chlorine K-edge; Sanchez-Valle, 2013). Furthermore,
82 among the halogens, bromine displays the closest behavior to chlorine in terms of solubility,
83 partitioning and speciation in silicate melts, at least at shallow depth (Bureau et al., 2000, Bureau
84 and Metrich, 2003; Wasik et al., 2005; Bureau et al., 2010; Cadoux et al., 2018). Bromine
85 therefore represents the best analog of Cl for *in-situ* studies at high pressure (*P*) and high
86 temperature (*T*) conditions. Our experimental results reveal systematic changes in Br speciation
87 that reflect changes in fluid composition with depth; these new findings enable better constraints
88 on the mechanisms controlling the transfer of halogens from the slab to arc magmas.

89

90 **2 Methods**

91 **2.1 Starting materials**

92 The speciation and fluid-melt partitioning experiments were conducted using 3 wt% NaBr
93 aqueous solutions and synthetic sodium disilicate (NS2: $\text{Na}_2\text{Si}_2\text{O}_5$) or haplogranite (Hpg) glasses
94 doped with 1 to 4 wt% Br as starting materials (Table 1). The 3 wt% NaBr aqueous solution was
95 freshly prepared from distilled de-ionized water and analytical grade NaBr powder, sealed in
96 tight containers and refrigerated until the experiments. The NS2 and Hpg glasses were
97 synthesized in a piston-cylinder apparatus at 1200 °C and 0.5 GPa and 1.5 GPa, respectively,
98 following the method described in Louvel et al. (2013). Briefly, reagent grade SiO_2 and Na_2SiO_3
99 were employed for the NS2 glasses whereas reagent grade SiO_2 , Al_2O_3 and alkali-carbonates,
100 K_2CO_3 and Na_2CO_3 , were mixed for the haplogranite glass synthesis. Bromine was added as
101 NaBr together with 3.3 wt% H_2O for the synthesis of the haplogranite glass to ensure complete
102 melting and homogeneization of the sample at run conditions.

103 Major element (Si, Al, K and Na) contents and distribution in the glass were measured by
104 by electron microprobe analyzer (EPMA) using a JEOL JXA-8200 microprobe with an

105 accelerating voltage of 15 keV, a 10 nA beam current and a defocused beam of 30 μm to avoid
106 element migration during the analysis (Table 1). The probe was calibrated using
107 wollastonite/quartz (Si), corundum (Al), aegirine (Na), K-feldspar (K), and counting time set to
108 40 s. The homogeneity of the glasses was confirmed by elemental profiles collected across the
109 sample and by the absence of microscopic mineral phases. EPMA measurements of Br are
110 hindered by i) the high ionization potential for the K-lines of Br resulting in low count rates; ii)
111 the peak overlap between the L-lines of Br and the K-lines of Al; and iii) the lack of matrix-
112 matched standards. To overcome these limitations, the concentration of Br in Hpg-Br2 glass
113 sample was first determined by Rutherford Backscattering Spectroscopy (RBS) at the
114 Department of Physics of ETH Zurich. This technique provides absolute elemental
115 concentrations and is particularly appropriated for quantifying heavy elements in a light matrix
116 as it is the case of Br in silicate glasses (Feldman and Mayer, 1986; Chu and Liu, 1996). A 3.5
117 mm diameter disk of Hpg-Br2 glass, mounted in epoxy and carbon-coated, was exposed to a 2
118 MeV ^4He ion beam. The concentration of Br in the sample was determined from the energy of
119 the backscattered alpha particles $^4\text{He}^{2+}$, yielding a Br concentration of 0.96 ± 0.04 wt%, which is
120 identical to the nominal Br concentration within analytical uncertainties (Table 1). This well-
121 characterized sample was then used as a standard for Br analysis by EPMA and LA-ICPMS in
122 the other glass samples (NS2 and Hpg-Br3 – Table 1). EPMA characterization of Br was
123 conducted with an accelerating voltage of 25 keV, a 90 nA beam current and a defocused beam
124 of 30 μm . The signal from Br (and Na) was carefully monitored during the measurements and
125 found to be stable for these conditions. Br concentrations in NS2-Br1 were also cross-checked by
126 LA-ICPMS analyses that were conducted using a 193-nm ArF excimer laser coupled with an
127 ELAN 6100 DRC ICP quadrupole mass spectrometer (Heinrich et al., 2003) and a beam

128 diameter of 40 μm . All analyses were bracketed by measuring an external standard (NIST 610)
129 to allow for linear drift correction, and the average SiO_2 and Br content determined by EPMA
130 analysis for the Hpg-Br2 glass was used as the internal standard.

131

132 **2.2 Hydrothermal diamond anvil cell experiments**

133 All experiments were conducted in Bassett-type hydrothermal diamond-anvil cells
134 (HDAC, Bassett et al., 1993) widely used for *in-situ* SXRF and XAS measurements on aqueous
135 fluids and silicate melts up to 1000 $^{\circ}\text{C}$ and about 3 GPa (e.g., Borchert et al., 2009; Louvel et al.,
136 2013, 2014). The HDAC were mounted with a thinner diamond (1.2-mm thick) on the detector
137 side to reduce the X-ray path through the diamonds and widen the collection angle of the XAS
138 analysis (Sanchez-Valle et al., 2004). This configuration permits i) to reduce the attenuation of
139 the fluorescence X-rays in the anvil, and ii) to lower the fluorescence background arising from
140 the Compton and Rayleigh scattering in the thick diamond anvils, hence increasing the signal to
141 noise ratio and thus the overall quality of the analysis. The sample chamber, a 300- μm hole
142 drilled in a 250- μm rhenium gasket compressed between the two diamond anvils, was heated
143 externally with molybdenum wires wrapped around two tungsten carbide seats supporting the
144 diamond anvils. Temperature was measured to within 2 $^{\circ}\text{C}$ with K-type thermocouples attached
145 to each anvil, as close as possible to the sample chamber. The temperature gradient between
146 thermocouples and the sample chamber was calibrated for each HDAC prior to experiments
147 using the melting temperature at ambient pressure of S (115.4 $^{\circ}\text{C}$), NaNO_3 (308.0 $^{\circ}\text{C}$) and NaCl
148 (800.5 $^{\circ}\text{C}$). Overall, the T gradient remains <35 $^{\circ}\text{C}$ at the highest temperature reached (850 $^{\circ}\text{C}$).
149 Pressure was determined from the equation of state of the gold internal pressure standard
150 (Jamieson et al., 1982) whose X-ray diffraction pattern was measured during the experiment.

151

152 Fluid-melt partitioning experiments were conducted by loading the sample chamber with a
153 piece of Br-bearing Hpg glass and either pure H₂O or an aqueous 3 wt% NaBr solution (Fig. 1).
154 For the speciation measurements by XAS, loadings included either Br aqueous solutions, or a
155 piece of Br-bearing NS2 or Hpg glass loaded together with de-ionized water. In all runs, a pellet
156 of a mixture of Au and Al₂O₃ powders was added to be used for pressure calibration (Louvel et
157 al., 2013; 2014). The volumetric proportions of glass and aqueous fluid in the different loadings
158 were adjusted by adding double-side polished glass pieces of known dimensions (Fig. 1). Upon
159 heating, the haplogranite melt-aqueous fluid system followed the classical phase transitions
160 described in previous studies (Bureau and Keppler, 1999; Louvel et al., 2013), with initial
161 hydrous melting recorded between 550 and 700 °C (Fig. 1B) and complete miscibility reached
162 within the 700-850 °C range, depending on the pressure (Fig. 1C). In contrast, the NS2-H₂O
163 system displayed distinct and rather unusual phase relations in the investigated *P-T* range (Fig.
164 1D-F): the NS2 glass first dissolved completely in the aqueous solution between 150 and 250 °C
165 to produce a single fluid phase containing 30 to 60 wt% dissolved Na₂O and SiO₂ solutes, an
166 analog for slab-derived so-called supercritical fluids (Fig. 1E). Upon further heating between 500
167 and 750 °C, the fluid unmixed into two phases, a hydrous melt and an aqueous fluid (Fig. 1F).
168 This immiscibility gap remained open up to the highest temperatures reached with the HDAC
169 (800-900 °C), as also previously observed for the haploandesite Na₂Si₄O₉-Na₂(Si,Al)₄O₉ join and
170 the K₂O-SiO₂-H₂O system (Mysen and Cody, 2004).

171 The composition of the high-pressure fluids (wt% cations dissolved) and melts (wt% H₂O)
172 was determined from available solubility studies (Table 2) as follows. The water content of
173 haplogranite melts at equilibrium with aqueous fluids (Fig. 1B) was calculated from the water

174 solubility data for aluminosilicate melts reported by Mysen and Wheeler (2000) and extrapolated
175 to our experimental conditions. The composition of the aqueous fluid phase in equilibrium with
176 the haplogranite melt (*i.e.*, total silicates content including SiO₂, Al₂O₃, Na₂O and K₂O) was
177 estimated by extrapolating to the *P-T* conditions of our experiments the solubility data reported
178 for the albite-H₂O system between 0.20 and 0.84 GPa at 600 and 700 °C (Anderson and
179 Burnham, 1983), except for Run 4, for which the high pressure (1-2 GPa) solubility data of
180 Wolhers et al. (2011) were employed. Uncertainties in the calculated dissolved silicate content
181 mostly arise from the compositional differences between solubility models (albite) and our
182 experimental system (peralkaline haplogranite), but they cannot be rigorously quantified here
183 due to a lack of information on Si, Na, K and Al partitioning between silicate melts and water.
184 To account for potential uncertainties on calculated silicate contents in the fluid phase we thus
185 considered a 10% error on pressure values, which translates to an overall uncertainty of 20-22%
186 for all investigated conditions, except in Run 4 (Table 2). The compositions of the aqueous fluids
187 in the NS2-H₂O system were determined from the initial volumetric proportions of the NS2 glass
188 and the aqueous fluid loaded in the compression chamber. The mass of the glass was calculated
189 from its measured volume using a density of 2.52(5) g/cm³ (Yamashita et al., 2008) and that of
190 the fluid determined from the volume left in the compression chamber (Fig. 1D). The amount of
191 water dissolved in the hydrous NS2 melt in equilibrium with the aqueous fluid at 700 °C and 0.4
192 GPa (Fig. 1F) was calculated from water solubility data in sodium silicate melts reported by
193 Mysen and Cody (2004). The overall error in the calculated bulk compositions is within 10% of
194 the total concentration value.

195

196 **2.3 *In-situ* SXRF and XAS measurements and data analysis**

197 The SXRF and XAS measurements were performed at the microXAS beamline (X05LA)
198 of the Swiss Light Source (SLS, Paul Scherrer Institute, Borca et al., 2009). Measurements at the
199 Br K-edge were conducted with an incident energy of 13.6 keV tuned by a Si(111) double crystal
200 monochromator and focused down to 5×8 (V×H) μm^2 size by a set of Rh-coated Kirkpatrick-
201 Baez mirrors. This configuration ensured a photon flux of 2×10^{11} photons per second at the
202 measurements conditions. The intensity of the incident beam was monitored throughout the
203 experiments using an Ar-filled micro-ion-chamber placed between the Kirkpatrick-Baez mirrors
204 and the HDAC. Before measurements, temperature was stabilized for about 30 min after each
205 heating stage to ensure that chemical equilibrium was achieved inside the cell (Louvel et al.,
206 2014). In the case of coexisting melt and fluid, measurements were only performed when the
207 melt globule was stationary and bridging both diamonds (Fig. 1F). This configuration ensured
208 that spectra were only collected from pure phases (fluid or melt) thus avoiding any
209 contamination of the SXRF and XAS signals by the other coexisting phase. SXRF and XAS
210 spectra were collected in fluorescence mode in a forward scattering geometry with an energy
211 dispersive single-element silicon drift diode (SDD) detector (Ketek[®], 139 eV resolution at Mn-K_α
212 = 5.89 keV) set at 22° from the incident beam in the horizontal plane (Sanchez-Valle et al., 2003;
213 Louvel et al., 2013; 2014). Angle-dispersive X-ray diffraction spectra were collected on the gold
214 pressure calibrant before and after XAS/SXRF measurements using a high-resolution CCD
215 camera set in transmission geometry. A microscope equipped with a video camera was used to
216 monitor the compression chamber during the heating and cooling cycles (Fig. 1).

217

218 2D-SXRF maps were acquired across the sample chamber to qualitatively monitor the
219 distribution of Br between the coexisting aqueous fluid and haplogranite melt (Fig. 1). Then, at

220 least three fluorescence spectra were collected from each phase to further determine the Br fluid-
 221 melt partition coefficients $D_{Br}^{f/m}$ at each P - T condition (Table 2). Counting times were set to 100
 222 or 300 s, depending on the signal intensity. Spectra were always recorded far away from the Au
 223 pressure calibrant (Fig. 2) to suppress the contribution of the Au L_{β} line (11.442 keV) to the Br
 224 K_{α} line (11.924 keV) used for the quantifications. Note that the Au L_{β} line was only observed in
 225 the spectra when the beam spot was positioned within less than 5 μm away from the Au chip
 226 (horizontal beam size 8 μm) thus demonstrating the well defined beam shape and appropriate
 227 spatial resolution of the X-ray beam.

228 The fluid-melt partition coefficients, $D_{Br}^{f/m}$, which correspond to the ratio of Br concentration in
 229 coexisting fluid (C_{Br}^f) and melt (C_{Br}^m) at each P - T , were derived from the integrated intensities of
 230 the Br fluorescence emission line recorded in the fluid and melt, I_f and I_m , after normalization to
 231 the incident beam intensity and counting times, and background removal with the Peakfit v4.12
 232 software (SeaSolve Software-USA), following the method described in Louvel et al. (2014). This
 233 method relies on the fixed geometry of the HDAC set-up and takes into account the different
 234 composition, density (ρ) and effective transmission (A) of the aqueous fluid and melt to
 235 normalize the fluorescence signal and calculate $D_{Br}^{f/m}$ according to the equation:

236

$$237 \quad D_{Br}^{f/m} = \frac{C_{Br}^f}{C_{Br}^m} = \frac{I_f}{I_m} \times \frac{A_m}{A_f} \times \frac{\rho_m}{\rho_f} \quad (1)$$

238

239 The standard deviation on the intensity ratios I_f/I_m is smaller than 10% (Table 2). The fluid and
 240 melt densities were calculated for the relevant pressure, temperature and fluid or melt
 241 compositions using density relations determined by *in situ* techniques for comparable fluid and

242 melt compositions by Mantegazzi et al. (2012) and Malfait et al. (2014) and **assuming a 10%**
243 **uncertainty on pressure determination and by propagating this error on the fluid and melt**
244 **compositions.** The effective transmission A_f and A_m , which accounts for the probability that the
245 fluorescent radiation reaches the detector depending on phase composition, density and thickness
246 of the sample at the incident energy, was calculated from the compositionally dependent
247 attenuation lengths λ determined below and above the Br K-edge energy as a function of
248 melt/fluid compositions and densities for all P - T conditions using the Hephaestus software
249 (Ravel and Newville, 2005). The sample thickness t was set as an average of the thickness of the
250 sample chamber after each run ($\sim 200 \mu\text{m}$). A variation of the sample thickness by $50 \mu\text{m}$
251 induces a deviation smaller than 10 % on the absolute value of the A_m/A_f ratio. Note that the
252 corrections in Eq. 1 significantly affect $D_{Br}^{f/m}$. Because the XRF intensities correlate with the Br
253 concentration and the melts are denser than the fluids, the values for $D_{Br}^{f/m}$ are consistently
254 higher than the I_f/I_m ratio itself (Table 2). **Partition coefficients derived in this study are**
255 **reported with 2σ uncertainty that takes into account the analytical uncertainty on the**
256 **intensity ratios I_f/I_m and an extra 10 % error on pressure determination and its**
257 **propagation on the fluid and melt compositions, densities and effective transmission.**

258
259 XAS measurements were conducted on 3 wt% NaBr aqueous solution, ‘solute-poor’ fluids
260 equilibrated with hydrous haplogranite melt (Fig. 1B), supercritical fluids containing different
261 amounts of dissolved NS2 (Fig. 1E) and hydrous NS2 melt (Fig. 1F). XAS analyses on the
262 haplogranite melt were precluded by the lower Br concentration of these melts ($< 0.2 \text{ wt}\%$). For
263 each composition, 3 to 5 XAS spectra were collected with counting times of 1 second per point
264 in the pre-edge region to 3 seconds in the XANES and EXAFS regions. The contribution of

265 Bragg reflections arising from the diamond anvils was avoided in the energy range of interest by
266 changing the orientation of the diamond anvil cell by 0.5 to 1° with respect to the incident X-ray
267 beam direction (Bassett et al., 2000). The edge position was calibrated using a pellet of NaBr and
268 no significant drift of the energy was observed during measurements. XAS spectra were also
269 collected at ambient conditions on ~ 200×200 μm² double-side polished section of the NS2 and
270 Hpg glasses.

271 Data reduction was performed using the Athena and Artemis packages (Ravel and
272 Newville, 2005) based on the IFEFFIT program (Newville, 2001). Averaged experimental
273 spectra were normalized to the absorption edge height and background removed using the
274 automatic background subtraction routine AUTOBK included in the Athena software. To
275 minimize the contribution of features at distances below the atom-atom contact distance, the R_{bkg}
276 parameter, which represents the minimum distance for which information is provided by the
277 signal, was set to 1.3 Å. For all spectra, the absorption energy E_0 was set to 13.474 keV, which
278 corresponds to the maximum of the first derivative of the absorption edge. Based on previous
279 studies of Br and Cl speciation in aqueous solutions and silicate glasses (Ayala et al., 2002;
280 D'Angelo et al., 1993; Evans et al., 2008; Ferlat et al., 2001; McKeown et al., 2011; Ramos et
281 al., 2000; Sandland et al., 2004; Stebbins and Du, 2002), our EXAFS analysis included the Br-O
282 and Br-Na scattering paths to describe the evolution of the local structure around Br from the
283 high P - T fluids to the hydrous melts and silicate glasses. Although Na cannot be easily
284 distinguished from Al or Si by EXAFS under our experimental conditions, the presence of
285 network cations in the nearest coordination shell of Br is deemed unlikely, as shown for Cl by
286 MAS-NMR and XAS studies (Evans et al., 2008; McKeown et al., 2011; Sandland et al., 2004;
287 Stebbins and Du, 2002). The theoretical back-scattering amplitudes, mean free-paths and phase-

288 shift functions for these paths were calculated with the FEFF6.0 *ab initio* code (Mustre de Leon
289 et al., 1991) using an aqueous Br ion $[\text{Br}(\text{H}_2\text{O})_6]^-$ with a mean Br-O distance of 3.37 Å and the
290 NaBr salt crystallographic structure with a Br-Na distance of 2.98 Å (Deshpande, 1961; Makino,
291 1995). Multiple scattering within a linear Br···H-O cluster was also included to model the
292 hydration shell around Br, with the H-O distance fixed to 1.0 Å (Silvestrelli and Parrinello, 1999;
293 Soper and Benmore, 2008). The $\chi(k)$ EXAFS function were Fourier filtered over the 1.5-6.0 Å⁻¹
294 *k*-range for most spectra. For all samples, modelling of the EXAFS oscillations was performed
295 using 4 variables: average coordination number (N), distance to nearest neighbor (R), Debye-
296 Waller factor σ^2 , and the energy shift ΔE (which is a non-structural parameter). The amplitude
297 reduction factor S_0^2 was set to 1 based on previous fits of aqueous NaBr, KBr and GaBr₃
298 solutions (Da Silva et al., 2009; Ferlat et al., 2002). All fits were performed simultaneously with
299 *k*-weighting of 1, 2 and 3 in order to decrease correlations between N and σ^2 , and R and ΔE
300 (Pokrovski et al., 2009a,b). The multi-electronic excitations (MEE) at 34 and 90 (± 1) eV above
301 the Br K-edge (D'Angelo et al., 1993) were neglected as they did not significantly contribute to
302 the EXAFS spectra. The variation of ΔE values between different fitted samples was less than \pm
303 4 eV, further confirming the validity of the fitting procedure and the accuracy of the derived
304 interatomic distances.

305

306 **3 RESULTS AND DISCUSSION**

307 **3.1 Bromine partition coefficients in the haplogranite-fluid system**

308 The distribution of Br between aqueous fluids and silicate melts at high *P-T* conditions
309 has been constrained by measuring fluid-melt partition coefficients $D_{\text{Br}}^{f/m}$ from 592 to 840 °C
310 and from 0.2 to 1.7 GPa in four experimental runs. For all investigated conditions, the $D_{\text{Br}}^{f/m}$

311 values are always higher than 1 (Table 2), confirming the preferential partitioning of Br into the
312 fluid phase, which is also qualitatively evident from the *in-situ* Br distribution maps reported in
313 Figure 2. The $D_{Br}^{f/m}$ values vary between 2.0 ± 0.1 and 15.3 ± 1.0 , and fall within the range
314 reported in a previous HDAC study by Bureau et al. (2010) at similar P - T conditions (Fig. 3).
315 Our limited set of $D_{Br}^{f/m}$ values does not display any clear and systematic pressure, composition
316 or density dependence (**Fig. 3B**) as it would generally be expected for vapor-liquid and fluid-
317 melt equilibrium partitioning of elements, which postulates that a partition coefficient should
318 tend to 1 when approaching the critical point at which the compositions and densities of both
319 phases are identical by definition (e.g., Bureau and Keppler, 1999; Pokrovski et al., 2013 and
320 references therein). **While such trend is indeed vaguely apparent for Runs 1 and 2, in which**
321 **the partition coefficients decrease with increasing P - T , Runs 3 and 4 do not show such**
322 **trend (Fig. 3A). The lack of pressure-density trend and the apparent data scatter might be**
323 **partially related to larger uncertainties on the pressure calibration when employing the**
324 **equation of state of gold at low pressures. Yet, large differences between Br chemical**
325 **speciation in the melt and fluid phases (see section 3.2) may also contribute to the apparent**
326 **data scatter, obscuring the simple water activity-, density- or pressure-dependent**
327 **partitioning trends as reported for vapor-liquid partitioning (Pokrovski et al., 2013), and,**
328 **ultimately, driving the system towards non-ideal, non-Henrian behavior, as for instance**
329 **reported for the fluid-melt partitioning of Cl under crustal magmatic conditions (cf. data**
330 **from Webster., 1992 in Fig. 3B). In this regard, the large $D_{Br}^{f/m} = 9.7$ obtained at 1.7 GPa in**
331 **Run 4, when the system should be close to miscibility and $D_{Br}^{f/m} \sim 1$ (Table 2, Fig. 3) may**
332 **result, at least partly, from differences between the real fluid composition and that**
333 **estimated using available data (Wohlert et al., 2011), coupled with possible non-Henrian**

334 effects, *i.e.*, ~ 2 wt% Br dissolved in the sample chamber compared to only ~0.5wt% for
335 Runs 1 to 3. We further note that previous *in-situ* high P - T measurements of $D_{Br}^{f/m}$ (Bureau
336 et al., 2010) also do not show clear P - T dependence for pressure > 0.6 GPa, e.g., $D_{Br}^{f/m} = 2.8$ -
337 6.4 between 625-655 °C at 1.2 GPa. Thus, the combined effect of pressure, temperature and
338 fluid and melt composition changes on Br fluid-melt partitioning should be more
339 systematically investigated at $P > 0.2$ GPa.

340 Despite the current uncertainties, an important observation here is that the $D_{Br}^{f/m}$ values remain
341 relatively small, 6.7 ± 3.6 (1σ), over a wide range of P - T conditions. Assuming that the high P - T
342 fluid/melt volumetric ratio is similar to the initial fluid/glass ratio for each run, we calculate
343 between 0.04 and 0.2 wt% Br to be dissolved in the high P - T hydrous melts at run conditions.
344 This estimation suggests that hydrous granitic melts have a capacity comparable to fluids to carry
345 Br under subduction-zone P - T conditions and may thus contribute to the efficient transport of Br
346 from the subducting slab to the mantle wedge and volcanic arc.

347
348 At lower-pressure conditions relevant to fore-arc or crustal processes (<0.2 GPa), our *in-situ*
349 partition coefficients are slightly lower than those obtained from quench experiments (Fig. 3).
350 For instance, Bureau et al. (2000) and Cadoux et al. (2018) reported average $D_{Br}^{f/m}$ of ~ 17-20
351 for albitic and rhyodacitic melts at 900 °C and 0.2 GPa, while we found $D_{Br}^{f/m}$ of ~ 5 at 800 °C
352 and 0.2 GPa. The minimum $D_{Br}^{f/m}$ value from Cadoux et al. (2018) is ~ 9, which is close to our
353 *in-situ* value. The small differences between our and the previous studies may stem from
354 uncertainties in the pressure determination below 0.5 GPa in the HDAC, the quantification of Br
355 by mass balance in Bureau et al. and Cadoux et al. (*i.e.* salt precipitates), or artifacts of the

356 quench method resulting in the loss of Br to the aqueous phase upon cooling in those ex-situ
357 studies. Furthermore, slight differences in the melt composition and structure could also result in
358 different Br speciation (Louvel et al., 2020), favoring or not the incorporation of Br in the silicate
359 melt. **The relatively low Br partition coefficients (< 20) compare favorably with those**
360 **reported for Cl in experiments conducted under Cl-undersaturated conditions (*i.e.*,**
361 **Webster., 1992 – experiments with less <0.01 wt% Cl in quenched glass, reported as solid**
362 **grey circles in Figure 3B). Nonetheless, comparison between these and our study underline**
363 **that additional efforts are yet required to quantitatively assess the effect of halogens contents**
364 **and density controls on Cl and Br fluid-melt partitioning (see Dolejs and Zajacz, 2018 and**
365 **Webster et al., 2018 for reviews).**

366

367 **3.2 Speciation of bromine in aqueous fluids and silicate melts**

368 **3.2.1 Aqueous solutions and silicate glasses at room conditions**

369 The XANES and EXAFS spectra collected at ambient conditions from the 3 wt% NaBr
370 aqueous solution and Br-bearing silicate glasses are reported respectively in Figures 4 and 5,
371 together with data for a KBr aqueous solution from Ferlat et al. (2002). These spectra were
372 employed to validate the theoretical backscattering amplitude and phase shift functions for Br-O
373 and Br-Na scattering paths used in EXAFS modeling. The XANES spectrum of the 3 wt% NaBr
374 aqueous solution is characterized by an absorption edge at 13.474 keV and a white line that
375 peaks at 13.478 keV (Fig. 4). It displays close similarities to that of the KBr aqueous solution
376 from Ferlat et al. (2002) and overall resembles other alkali bromide aqueous solutions reported in
377 the literature (Wallen et al., 1997; Ferlat et al., 2001; Evans et al., 2007). The EXAFS spectra
378 from the KBr and NaBr aqueous solutions are accurately modeled with a hydration shell of $5.7 \pm$

379 0.8 and 5.9 ± 0.7 water molecules ($N_{\text{Br}\cdots\text{H-O}}$) at a Br-O distance of 3.30 ± 0.03 and 3.37 ± 0.04 Å,
380 respectively (Table 3). Note that multiple-scattering paths from the linear Br \cdots H-O cluster are
381 needed to accurately reproduce the experimental data; when only Br-O interactions are
382 considered, the model fails to reproduce the amplitude of the EXAFS oscillations unless an
383 unrealistic hydration shell of ~ 12 H₂O molecules is adopted. The structural parameters fitted for
384 the KBr aqueous solution from Ferlat et al. (2002) are, within errors, similar to those reported by
385 the authors. Together with the EXAFS fits of the NaBr aqueous solution, they confirm that Br
386 speciation in aqueous solution at room conditions is dominated by a six-fold coordinated
387 hydration shell with the H-O bond of the water molecule radially aligned towards the Br ion
388 (Ferlat et al., 2001; Ramos et al., 2000).

389 EXAFS spectra collected on NS2 and Hpg glasses at room conditions display distinct
390 oscillations, with a new feature at 2.2 \AA^{-1} in both glass samples and amplitudes nearly out of
391 phase at $> 2 \text{ \AA}^{-1}$ in k -space compared to the NaBr and KBr aqueous solutions (Fig. 6). Different
392 combinations of Br-Na and Br-O scattering paths were tested to constrain the local structural
393 environment of Br in the silicate glasses. Models considering individually either the Br-Na or Br-
394 O paths do not provide a reasonable fit of the EXAFS oscillations and the simultaneous
395 contribution of Br-Na and Br-O bond is required to reproduce the experimental spectra. The
396 EXAFS-derived parameters suggest that Br in NS2 and Hpg glasses is coordinated to an average
397 of 6 Na cations in the first shell at an average distance of 2.95 \AA , and next-nearest 6 O neighbors
398 located at 3.4 \AA (Table 3). The fitted Br-Na bond length is consistent, within errors, with
399 theoretical Br-Na distances in crystalline NaBr (2.987 \AA , Deshpande, 1961) and is close to that
400 reported for aluminosilicate glasses in a previous study (Cochain et al., 2015), suggesting Br is
401 incorporated in the silicate glasses in a “salt-like” structure, similar to NaBr. The similarities

402 between the structural parameters fitted for anhydrous NS2 and hydrous Hpg (3.3 wt% H₂O)
403 glasses also suggest that the nearest environment of Br remains largely anhydrous in glasses
404 containing relatively low water contents and that the second O neighbors may be from the
405 silicate network rather than more distant H₂O or OH groups. Attempts to include the effect of
406 Br···H-O bonds in the fitting model by taking into account multiple scattering Br···H-O paths
407 instead of Br-O correlations only resulted in a systematic decrease in the fit quality (higher *R*-
408 factor). The sole difference between the two glasses is the presence of a pre-edge feature at
409 ~13.468 keV in the haplogranite glass (Fig. 5). Such features have been attributed to the 1s to 4p
410 electronic transitions in Br (Burattini et al., 1991) and reported in several covalently bonded
411 and/or reduced Br-bearing compounds, including HBr, Br₂, and CHBr₃ (D'Angelo et al., 1993;
412 Feiters et al., 2005). While Evans et al. (2007) suggested that this feature could arise from partial
413 Br reduction in the presence of remaining carbon material in the sample from the synthesis,
414 changes in the local site symmetry around Br could also contribute to the development of such
415 feature. Recent HERFD-XAS measurements conducted on silicate glasses however demonstrate
416 that this feature is absent in basaltic and andesitic glasses and hence, may be specific to the
417 structure of granitic glass compositions (Louvel et al., 2020).

418

419 **3.2.2 High *P-T* aqueous fluids and hydrous silicate melts**

420 Bromine K-edge XANES spectra of high *P-T* aqueous fluids (3 wt% NaBr solution,
421 fluids at equilibrium with haplogranite melt and water-dominated fluids containing < 50 wt%
422 dissolved NS2) all share a shape very similar to that of the NaBr aqueous solution at room
423 conditions, suggesting a similar local structure of Br in H₂O-dominated phases at elevated *P-T*
424 (Fig. 4 and 5). Differences in the shape of the XANES spectra become more pronounced for the

425 supercritical fluids with >50 wt% dissolved Si and Na and the hydrous NS2 melt (Fig. 4).
426 Although the maximum of the white line remains at 13.478 keV, it broadens and decreases in
427 amplitude compared to the 3 wt% NaBr aqueous solution. Also, the first post-edge resonance is
428 shifted toward either higher (13.504 keV) or lower (13.487 keV) energies compared to the
429 aqueous fluids. These changes may be indicative of the progressive incorporation of Na in the
430 local structure around Br. These modifications of Br coordination environment are also
431 noticeable in the EXAFS oscillations (Fig. 5): while Br-bearing aqueous fluids mostly show a
432 decrease of the amplitude of the oscillations with increasing P - T , they are shifted to higher
433 distances (*i.e.* from 2.6 to 2.8 Å⁻¹ in k -space for the first oscillation) for the 60 wt% NS2 fluid.
434 Moreover, the NS2 melt bears closer resemblance to the NS2 and Hpg glasses, sharing similar
435 oscillations at 2.2 and 3.2 Å⁻¹.

436 The structural parameters derived from the quantitative EXAFS analysis are reported in
437 Table 4. Comparably to room conditions, the EXAFS spectra of the NaBr aqueous solution at
438 high pressure-temperature conditions are well matched by an octahedral hydration shell
439 including multiple-scattering contributions from the Br···H-O cluster (Fig. 6). Br-O coordination
440 numbers and distances are, respectively, 6.4 ± 1.1 and 3.40 ± 0.07 Å at 450 °C and 0.6 GPa,
441 indicating the persistence of the 6-fold coordinated hydration shell up to high temperatures. This
442 observation contrasts with results from a number of classical EXAFS studies performed at lower
443 pressures (< 0.07 GPa at 450 °C) that reported significant reduction in the number of water
444 molecules around Br at supercritical conditions (Wallen et al., 1997; Da Silva et al., 2009). These
445 differences are likely to reflect the differences in pressure (or fluid density), with higher
446 pressures stabilizing the hydration shell around Br due to the increase in the solvent dielectric
447 constant (Pan et al., 2013; Sverjensky et al., 2014), as also predicted for other ions such as Li⁺

448 (Jahn and Wunder, 2009) and Ti^{4+} (van Sijl et al., 2010) by molecular dynamics simulations. An
449 exception to this trend are the experimental results of Mayanovic et al. (2001), who reported a
450 decrease by $> 60\%$ of the number of water molecules in the solvation shell of both Br aqua ions
451 and ZnBr_4^{2-} complexes in 1 m ZnBr_2 - 6 m NaBr aqueous solution from ambient conditions to
452 500 °C and 0.5 GPa. The reason for this discrepancy is unclear at this state of our knowledge and
453 additional studies on the speciation of Br in aqueous electrolytes will be necessary to explain the
454 disagreement.

455 There are no significant changes in Br speciation in the aqueous fluids equilibrated with
456 haplogranitic melts, which contain only few wt% of dissolved silicate components, and in fluids
457 containing up to 30 wt% dissolved NS2 (Fig. 6; Table 4). The first noticeable changes are only
458 found for fluids containing at least 50 wt% dissolved NS2, with a small decrease of the average
459 Br coordination number ($N_{\text{Br}\dots\text{H}_2\text{O}}$) to ~ 4.7 compared to more dilute fluids (~ 6.0). While this
460 value stays within errors from the other compositions, the reduction of the hydration shell might
461 define the onset of Br-Na complexation with increasing amount of Na dissolved in the fluid. This
462 hypothesis was tested by introducing a Br-Na contribution in the fitting model for the high
463 temperature data, but this resulted in a decrease of the overall fit quality. The formation of Br-Na
464 complexes and the partial dehydration of Br, however, becomes evident with further increase of
465 the solute content to 60 wt% dissolved NS2 in the fluid (Table 4). For this composition, the best-
466 fit model is consistent with the presence of ~ 3 Na atoms and 4 to 5 H_2O molecules (or OH
467 groups) in the nearest environment of Br, at 480 °C and 1.5 GPa and 610 °C and 2.2 GPa. In the
468 NS2 hydrous melt (10 wt% H_2O), the number of Na neighbors further increases to ~ 6 whereas
469 the number of oxygens remains similar to that of the 60 wt% NS2 fluid (~ 3.4). This increase in
470 the number of Na neighbors compared to the 60 wt% NS2-bearing fluid suggests that the nearest

471 environment of Br in silicate-rich fluids progressively approaches the local structure observed in
472 the NS2 glass. Yet, the Br local environment remains hydrated, in contrast to the NS2 and Hpg
473 glasses. Based on results from FTIR and ^{29}Si NMR studies showing that molecular H_2O is
474 favored in aluminosilicate and sodium silicate glasses as the amount of dissolved water increases
475 (Stolper, 1982; Uchino et al., 1992; Xue and Kanzaki, 2004; Behrens and Yamashita, 2008), we
476 suggest that molecular H_2O , rather than OH groups, would be present around Br in the hydrous
477 NS2 melt. Moreover, we cannot exclude that distinct “fluid-like” $\text{Br}(\text{H}_2\text{O})_6$ and “glass-like”
478 BrNa_6 complexes coexist in the hydrous melt as $[\text{yBr}(\text{H}_2\text{O})_6 + \text{xBrNa}_6]$ moieties, as the average
479 signal of these structures could not be distinguished from $[\text{BrNa}_y(\text{H}_2\text{O})_x]$ clusters by XANES or
480 EXAFS. Although Br speciation could not be investigated in the hydrous haplogranite melt due
481 to lower Br concentrations (< 0.2 wt%), the similarities between both XANES and EXAFS
482 spectra of the Hpg and NS2 glasses (Fig. 4 and 5) allow us to anticipate a similar Br local
483 environment in the haplogranite melt, dominated by alkali complexation.

484

485 **4. Implications for the transport and recycling of halogens in subduction zones**

486 The new partitioning and speciation data derived for bromine in the present study provide
487 direct insights on the transport mechanisms of halogens (Cl, Br and I) in subduction zones. Our
488 results suggest that the mobilization of Br (and likely Cl, Br and I) in subduction zones is
489 affected by the chemistry of the slab-derived mobile phases. These phases, in turn, are essentially
490 controlled by the slab composition and the depth of fluid extraction and hence, by the P - T
491 conditions (Schmidt and Poli, 1998; Manning, 2004; Schmidt et al., 2004; Hermann et al., 2006;
492 Bebout, 2007; Keppler, 2017). Figure 6 illustrates a gradual transition of Br speciation from
493 hydrated species $[\text{Br}(\text{H}_2\text{O})_6]^-$ to $[\text{BrNa}_x(\text{H}_2\text{O})_y]$ clusters with various stoichiometries (or mixture

494 of $[\text{Br}(\text{H}_2\text{O})_6]$ and BrNa_6 moieties) as the fluid composition evolves from diluted aqueous fluids
495 such as those released by continuous metamorphic dehydration of the slab (< 15 wt% dissolved
496 solutes, Manning, 2004; Rustioni et al., 2019) to Si/Na-rich supercritical fluids that form owing
497 to enhanced solubility of silicate minerals at depth and/or granitic melts produced by fluid-
498 assisted melting of subducted sediments (Hermann et al., 2006; Skora and Blundy, 2010). The
499 increasing similarities in the local structure of Br in aqueous fluids containing large amounts of
500 dissolved alkali-silica (> 12.5 wt% Na) and the hydrous melts (Fig. 6) is consistent with the
501 progressive decrease in the Br fluid-melt partition coefficients ($D_{\text{Br}}^{f/m}$) with T increase observed
502 in this study in each separated runs (Fig. 3). Sodium complexation with Br is thus an efficient
503 mechanism that enables not only aqueous fluids but also supercritical fluids and hydrous melts to
504 carry significant amounts of Br at depth.

505 General similarities between Cl, Br and I speciation in aqueous solutions and silicate
506 glasses (Evans et al., 2008; McKeown et al., 2011,2015; Shermann et al., 2010) suggest that the
507 speciation and partitioning trends found in our study for Br may extend to Cl and I. Therefore,
508 while early dehydration fluids should release large amounts of halogens to the fore-arc and the
509 mantle wedge (100 – 200 km depth), hydrous slab melts and supercritical fluids play a critical
510 role in recycling the residual halogens dragged by the subducting slabs to greater depths. Such
511 efficient recycling, where most of the Cl and Br subducted is transferred to the mantle wedge and
512 ultimately returned to the surface through arc magmatism, is further supported by recent
513 quantification of halogens in subducted sediments, serpentinites and altered oceanic crust. Mass
514 balance calculations indeed show a close match, within errors, between worldwide influx to the
515 mantle wedge, $\sim 13\text{-}15 \times 10^3$ kt/yr Cl and 5-70 kt/yr Br, and calculated outflux as HCl and HBr at
516 volcanic arcs, $\sim 3\text{-}22 \times 10^3$ kt/yr Cl and 5-15 kt/yr Br (Barnes et al., 2018; Chavrit et al., 2016;

517 Kendrick et al., 2013; Pyle and Mather, 2009). In comparison, iodine degassing at volcanic arcs
518 is less well constrained, making it more difficult to assess its fate in the subduction factory (e.g.,
519 Bureau et al., 2016). The small imbalances remaining between Cl and Br input and output fluxes
520 may arise from difficulties in quantifying halogen loss to the fore-arc and crustal hydrothermal
521 systems. Recent reports of halogens enrichment in oceanic islands basalts (Barnes et al., 2018;
522 Hanyu et al., 2019; Kendrick et al., 2017) also point to the subduction of a noticeable fraction of
523 F, Cl, Br and I to greater depth, to an extent that is yet to be quantified. **Additional in-situ**
524 **experiments, like those presented here, may help better constrain the mechanisms of halogen**
525 **transfert and partitioning at depth, which are inaccessible to direct observation.**

526

527 **5. Conclusions**

528 *In-situ* SXRF and XAS have been applied to quantify Br fluid-melt partition coefficients
529 and speciation in aqueous fluids, supercritical fluids and hydrous silicate melts up to 840 °C and
530 2.2 GPa. Above all, our experimental results demonstrate how changes in speciation, from
531 hydrated ions in aqueous fluids to ‘salt-like’ structures in hydrous melts, may facilitate the
532 uptake of high amounts of Cl, Br and, probably, I by subduction zone fluids, regardless of their
533 composition. Significant efforts are, however, still needed to accurately quantify halogen cycling
534 from the surface to the deep Earth and back. Especially, new experiments investigating the
535 solubility of halogens in subduction zone fluids and the capacity of high-pressure minerals (e.g.,
536 micas, Ti-clinohumite, apatite, and carbonates) to incorporate these elements are still necessary
537 to evaluate the amounts of halogen that may be returned to the volcanic arc or retained in the
538 slab.

539 **Acknowledgements:** This work was supported by the Swiss National Science Foundation
540 (grants 200021-120575 and 200020-132208 to CSV) and by the Swiss Academy of Sciences
541 (SATW) and the Ministères des Affaires étrangères et européennes (MAEE) et de
542 l'Enseignement Supérieur et de la Recherche (MESR) through the Partenariat Hubert Curien
543 (PHC). We thank M. Doebeli and J. H. Seo for conducting the RBS and LA-ICPMS analysis,
544 respectively. The Paul Scherrer Institute (PSI) and the Swiss Light Source (SLS) are
545 acknowledged for providing beamtime for the experiments. **Two anonymous reviewers and the**
546 **Topical Editor N. Malaspina are thanked for their help in improving the clarity of the**
547 **article.**

548

549 **References**

550 Anderson, G. M. and Burnham, C. W.: Feldspar solubility and the transport of aluminum under
551 metamorphic conditions. *Am. J. Sci.* 283, 283-297, 1983.

552 Ayala, R., Martinez, J. M., Pappalardo, R. R., Saint-Martin, H., Ortega-Blake I. and Sanchez-Marcos, E.:
553 Development of first-principles interaction model potentials. An application to the study of the
554 bromide hydration. *J. Chem. Phys.* **117**, 10512, 2002.

555 Barnes, J., Manning, C.E., Scambelluri, M. and Selverstone, J.: The behaviour of halogens during
556 subduction-zone processes. In D.E. Harlov and L. Aranovich (eds.), *The Role of Halogens in*
557 *Terrestrial and Extraterrestrial Geochemical Processes*, Springer Geochemistry, 545-590, 2018.

558 Bassett, W. A., Shen, A. H., Bucknum, M., and Chou, I. M.: A New Diamond-Anvil Cell for
559 Hydrothermal Studies to 2.5 GPa and from – 190 °C to 1200 °C. *Rev. Sci. Instrum.* 64, 2340-2345,
560 1993.

561 Bassett, W. A., Anderson, A. J., Mayanovic, R. A., and Chou, I.-M.: Hydrothermal diamond anvil cell for
562 XAFS studies of first-row transition elements in aqueous solution up to supercritical conditions.
563 Chem. Geol. 167, 3-10, 2000.

564 Bebout, G. E.: Metamorphic chemical geodynamics of subduction zones. Earth Planet. Sc. Lett. 260, 373-
565 393, 2007.

566 Behrens, H. and Yamashita, S.: Water speciation in hydrous sodium tetrasilicate and hexasilicate melts:
567 Constraint from high temperature NIR spectroscopy. Chem. Geol. 256, 306-315, 2008.

568 Bobrowski, N., Honninger, G., Galle, B., and Platt, U.: Detection of bromine monoxide in a volcanic
569 plume. Nature 423, 273-276, 2003.

570 Borca, C. N., Grolimund, D., Willmann, M., Meyer, B., Jefimovs, K., Vila-Comamala, J., and David, C.:
571 The microXASbeamline at the Swiss Light Source: towards nano-scale imaging. J. Phys. Conf. Ser.
572 186, 1-3, 2009.

573 Borchert, M., Wilke, M., Schmidt, C., and Rickers, K.: Partitioning and equilibration of Rb and Sr
574 between silicate melts and aqueous fluids. Chem. Geol. 259, 39-47, 2009.

575 Burattini, E., D'Angelo, P., Giglio, E. and Pavel, N.V.: EXAFS study of probe molecules in micellar
576 solutions. J. Phys. Chem. 95, 7880-7886, 1991.

577 Bureau, H. and Keppler, H.: Complete miscibility between silicate melts and hydrous fluids in the upper
578 mantle: experimental evidence and geochemical implications. Earth Planet. Sc. Lett. 165, 187-196,
579 1999.

580 Bureau, H. and Métrich, N.: An experimental study of bromine behaviour in water-saturated silicic melts.
581 Geochim. Cosmochim. Ac. 67, 1689-1697, 2003.

582 Bureau, H., Keppler, H., and Metrich, N.: Volcanic degassing of bromine and iodine: experimental
583 fluid/melt partitioning data and applications to stratospheric chemistry. Earth Planet. Sc. Lett. 183,
584 51-60, 2000.

585 Bureau, H., Foy, E., Raepsaet, C., Somogyi, A., Munsch, P., Simon, G., and Kubsky, S.: Bromine cycle in
586 subduction zones through in situ Br monitoring in diamond anvil cells. *Geochim. Cosmochim. Ac.*
587 74, 3839-3850, 2010.

588 Bureau, H., Auzende A-L., Marocchi, M., Raepsaet, C., Munsch, P., Testemale, D., Mezouar, M.,
589 Kubsky, S., Carriere, M., Ricolleau, A. and Fiquet, G.: Modern and past volcanic degassing of
590 iodine. *Geochim. Cosmochim. Ac.* 173, 114-125, 2016.

591 Cadoux, A., Iacono-Marziano, G., Scaillet, B., Aiuppa, A., Mather, T.A., Pyle, D.M., Deloule, E.,
592 Gennaro, E. and Paonita, A.: The role of melt composition on aqueous fluid vs. silicate melt
593 partitioning of bromine in magmas. *Earth Planet. Sc. Lett.* 498, 450-463, 2018.

594 Carroll, M. R.: Chlorine solubility in evolved alkaline magmas. *Annals of Geophysics* 48, 619-631, 2005.

595 Chavrit, D., Burgess, R., Sumino, H., Teagle, D.A.H., Droop, G., Shimizu, A. and Ballentine, C.J.: The
596 contribution of the hydrothermal alteration of the ocean crust to the deep halogen and noble gas
597 cycles. *Geochim. Cosmochim. Ac.* 183, 106-124, 2016.

598 Chu, W. K. and Liu, J. R.: Rutherford backscattering spectrometry: Reminiscences and progresses. *Mat.*
599 *Chem. Phys.* 46, 183-188, 1996.

600 Cochain, B., Sanloup, C., de Grouchy, C., Crepisson, C., Bureau, H., Leroy, C., Kantor, I., Irifune, T.:
601 Bromine speciation in hydrous silicate melts at high pressure. *Chem. Geol.* 404, 18-26, 2015.

602 D'angelo, P., Dicicco, A., Filipponi, A., and Pavel, N. V.: Double-electron excitation channels at th Br K-
603 edge of HBr and Br₂. *Phys. Rev. A* 47, 2055-2063, 1993.

604 Da Silva, C., Proux, O., Hazemann, J. L., James-Smith, J., Testemale, D., and Yamaguchi, T.: X-ray
605 absorption spectroscopy study of solvation and ion-pairing in aqueous gallium bromide solutions at
606 supercritical conditions. *J. Mol. Liq.* 147, 83-95, 2009

607 Deshpande, V.: Thermal Expansion of Sodium Fluoride and Sodium Bromide. *Acta Crystallogr.* 14, 794,
608 1961.

609 Dolejs, D. and Zajacz, Z.: Halogens in silicic magmas and their hydrothermal systems. In D.E. Harlov
610 and L. Aranovich (eds.), *The Role of Halogens in Terrestrial and Extraterrestrial Geochemical*
611 *Processes*, Springer Geochemistry, 431-543, 2018.

612 Evans, K. A., Mavrogenes, J., and Newville, M.: The effect of CO₂ on the speciation of bromine in low-
613 temperature geological solutions: an XANES study. *J. Synchrotron Radiat.* 14, 219-226, 2007.

614 Evans, K. A., Mavrogenes, J. A., O'Neill, H. S., Keller, N. S., and Jang, L. Y.: A preliminary
615 investigation of chlorine XANES in silicate glasses. *Geochem. Geophys. Geosy.* 9, Q10003,
616 doi:10.1029/2008GC002157, 2008.

617 Evans, K.A., Gordon, R.A., Mavrogenes, J.A. and Tailby, N.: The effect of CO₂ on the speciation of
618 RbBr in solution at temperatures to 579 °C and pressures to 0.26 GPa. *Geochim. Cosmochim. Ac.*
619 73, 2631-2644, 2009.

620 Feldman, L. C. and Mayer, J. W.: *Fundamentals of Surface and Thin Film Analysis*. Prentice Hall. pp
621 352, 1986.

622 Ferlat, G., San Miguel, A., Jal, J. F., Soetens, J. C., Bopp, P. A., Daniel, I., Guillot, S., Hazeman, J. L.,
623 and Argoud, R.: Hydration of the bromine ion in a supercritical 1 : 1 aqueous electrolyte. *Phys.*
624 *Rev. B* 63, 2001.

625 Ferlat, G., San Miguel, A., Jal, J. F., Soetens, J. C., Bopp, P. A., Hazemann, J. L., Testemale, D., and
626 Daniel, I.: The quest for ion pairing in supercritical aqueous electrolytes. *J. Mol. Liq.* 101, 127-136,
627 2002.

628 Frezzotti, M.L. and Ferrando, S.: The chemical behavior of fluids released during deep subduction based
629 on fluid inclusions. *Am. Mineral.* 100, 352-377, 2015.

630 Grutzner, T., Klemme, S., Rohrbach, A., Gervasoni, F. and Berndt, J.: The role of F-clinohumite in
631 volatiles recycling processes in subduction zones. *Geology* 45, 443-446, 2017.

632 Hanyu, T., Shimizu, K., Ushikubo, T., Kimura, J-I., Chang, Q., Hamada, M., Ito, M., Iwamori, H. and
633 Ishikawa, T.: Tiny droplets of ocean island basalts unveil Earth's deep chlorine cycle. *Nat.*
634 *Commun.* 10:60. <https://doi.org/10.1038/s41467-018-07955-8>, 2019.

635 Heinrich, C. A., Pettke, T., Halter, W. E., Aigner-Torres, M., Audéat, A., Günther, D., Hattendorf, B.,
636 Bleiner, D., Guillong, M., and Horn, I.: Quantitative multi-element analysis of minerals, fluid and
637 melt inclusions by laser-ablation inductively-coupled-plasma mass-spectrometry. *Geochim.*
638 *Cosmochim. Ac.* 67, 3473-3497, 2003.

639 Hermann, J., Spandler, C., Hack, A. and Korsakov, A.V.: Aqueous fluids and hydrous melts in high-
640 pressure and ultra-high pressure rocks: Implications for element transfer in subduction zones.
641 *Lithos* 92, 399-417, 2006.

642 Ikemoto, A. and Iwamori, H.: Numerical modeling of trace element transportation in subduction zones :
643 implications for geofluid processes. *Earth Planets Space* 66:26, 1-10, 2014.

644 Jahn, S. and Wunder, B.: Lithium speciation in aqueous fluids at high P and T studied by ab initio
645 molecular dynamics and consequences for Li-isotope fractionation between minerals and fluids.
646 *Geochim. Cosmochim. Ac.* 73, 5428-5434, 2009.

647 Jamieson, J. C., Fritz, J. N., and Manghnani, M. H.: Pressure measurement at high temperature in X-ray
648 diffraction studies: gold as a primary standard in High-Pressure Research in Geophysics, pp 27-48.
649 Center for Academic Publishing, Tokyo, 1982.

650 John, T., Scambelluri, M., Frische, M., Barnes, J. D., and Bach, W.: Dehydration of subducting
651 serpentinite: Implications for halogen mobility in subduction zones and the deep halogen cycle.
652 *Earth Planet. Sc. Lett.* 308, 65-76, 2011.

653 Kendrick, M.A., Honda, M., Pettke, T., Scambelluri, M., Phillips, D. and Giuliani, A.: Subduction zone
654 fluxes of halogens and noble gases in seafloor and forearc serpentinites. *Earth Planet. Sc. Lett.* 365,
655 86-96, 2013.

656 Kendrick, M.A., Honda, M. and Vanko, D.A.: Halogens and noble gases in Mathematician Ridge meta-
657 gabbros, NE Pacific: implication for oceanic hydrothermal root zones and global volatile cycles.
658 *Contrib. Mineral. Petr.* 170:43, 2015.

659 Kendrick, M.A., Hemond, C., Kamenetsky, V.S., Danyushevsky, L., Devey, C.W., Rodemann, T.,
660 Jackson, M.G. and Perfit, M.R.: Seawater cycled throughout Earth's mantle in partially
661 serpentinitized lithosphere. *Nat. Geosci.* 10, 222-229, 2017.

662 Kendrick, M.A., Scambelluri, M., Hermann, J. and Padron-Navarta, J.A.: Halogens and noble gases in
663 serpentinites and secondary peridotites: Implications for seawater subduction and the origin of
664 mantle neon. *Geochim. Cosmochim. Ac.* 235, 285-304, 2018.

665 Keppler, H.: Fluids and trace element transport in subduction zones. *Am. Mineral.* 102, 5-20, 2017.

666 Kimura, J-I., Gill, J-B., Skora, S., van Keken, P.E. and Kawabata, H.: Origin of geochemical mantle
667 components: Role of subduction filter. *Geochem. Geophys. Geosy.* 17, 3289-3325, 2016.

668 Louvel, M., Sanchez-Valle, C., Malfait, W.J., Testemale, D. and Hazemann, J-L.: Zr complexation in
669 high pressure fluids and implications for the mobilization of HFSE in subduction zones. *Geochim.*
670 *Cosmochim. Ac.* 104, 281-299, 2013.

671 Louvel, M., Sanchez-Valle, C., Malfait, W.J., Testemale, D. and Hazemann, J-L.: Constraints on the
672 mobilization of Zr in magmatic-hydrothermal processes in subduction zones from in situ fluid-melt
673 partitioning experiments. *Am. Mineral.* 99, 1616-1625, 2014.

674 Louvel, M., Cadoux, A., Brooker, R., Proux, Olivier and Hazemann, J-L.: New insights on Br speciation
675 in volcanic glasses and structural controls on halogens degassing. *In press, Am. Mineral., 2020,*
676 *10.2138/am-2020-7273*

677 Makino, Y.: Correlation between Pseudopotential Radii and Interatomic Distance and Evaluation of Bond
678 Characters for Transition and Lanthanide Elements. *J. Alloy. Compd.* 227, 18-27, 1995.

679 Manning, C. E.: The chemistry of subduction-zone fluids. *Earth Planet. Sc. Lett.* 223, 1-16, 2004.

680 Mayanovic, R. A., Anderson, A. J., Bassett, W. A., and Chou, I. M.: Hydrogen bond breaking in aqueous
681 solutions near the critical point. *Chem. Phys. Lett.* 336, 212-218, 2001.

682 McKeown, D. A., Gan, H., Pegg, I. L., Stolte, W. C., and Demchenko, I. N.: X-ray absorption studies of
683 chlorine valence and local environments in borosilicate waste glasses. *J. Nucl. Mater.* 408, 236-
684 245, 2011.

685 McKeown, D.A., Muller, I.S. and Pegg, I.L.: Iodine valence and local environments in borosilicate waste
686 glasses using X-ray absorption spectroscopy. *J. Nucl. Mater.* 456, 182-191, 2015.

687 Mustre de Leon, J., Rehr, J. J., Zabinsky, S. I., and Albers, R. C.: Ab initio curved-wave X-ray-absorption
688 fine structure. *Phys. Rev. B* 44, 4146-56, 1991.

689 Mysen, B. O. and Cody, G. D.: Solubility and solution mechanism of H₂O in alkali silicate melts and
690 glasses at high pressure and temperature. *Geochim. Cosmochim. Ac.* 68, 5113-5126, 2004.

691 Mysen, B.O. and Wheeler, K.: Solubility behavior of water in haploandesitic melts at high pressure and
692 high temperature. *Am. Mineral.* 85, 1128-1142, 2000.

693 Newville, M.: EXAFS analysis using FEFF and FEFFIT. *J. Synchrotron Radiat.* 8, 96-100, 2001.

694 Pan, D., Spanu, L., Harrison, B., Sverjensky, D.A. and Galli, G.: Dielectric properties of water under
695 extreme conditions and transport of carbonates in the deep Earth. *PNAS* 110, 6646-6650, 2013.

696 Pokrovski, G. S., Tagirov, B. R., Schott, J., Hazemann, J. L., and Proux, O.: A new view on gold
697 speciation in sulfur-bearing hydrothermal fluids from in situ X-ray absorption spectroscopy and
698 quantum-chemical modeling. *Geochim. Cosmochim. Ac.* 73, 5406-5427, 2013.

699 Pokrovski, G. S., Tagirov, B. R., Schott, J., Bazarkina, E. F., Hazemann, J. L., and Proux, O.: An in situ
700 X-ray absorption spectroscopy study of gold-chloride complexing in hydrothermal fluids. *Chem.*
701 *Geol.* 259, 17-29, 2009b.

702 Pokrovski G.S., Borisova A.Y., Bychkov A.Y.: Speciation and transport of metals and metalloids in
703 geological vapors. Book chapter 6 in: *Thermodynamics of Geothermal Fluids* (eds. A. Stefánsson,
704 T. Driesner, P. Bénézech). *Rev. Miner. Geochem.* 76, 165-218, 2013.

705 Poli, S. and Schmidt, M.W.: Petrology of subducted slabs. *Annu. Rev. Earth Planet. Sci.* 30, 207-235,
706 1998

707 Pyle, D. M. and Mather, T. A.: Halogens in igneous processes and their fluxes to the atmosphere and
708 oceans from volcanic activity: A review. *Chem. Geol.* 263, 110-121, 2009.

709 Ramos, S., Barnes, A. C., Neilson, G. W., Thiaudiere, D., and Lequien, S.: The hydration structure of Br-
710 from anomalous x-ray diffraction. *J. Phys.-Condens. Mat.* 12, A203-A208, 2000.

711 Ravel, B. and Newville, M.: ATHENA, ARTEMIS, HEPHAESTUS: data analysis for X-ray absorption
712 spectroscopy using IFEFFIT. *J. Synchrotron Radiat.* 12, 537-541, 2005.

713 Roberge, M., Bureau, H., Bolfan-Cassanova, N., Frost, D.J., Raepsaet, C., Surble, S., Khodja, H.,
714 Auzende, A-L. and Fiquet, G.: Is the transition zone a deep reservoir for fluorine? *Earth Planet. Sc.*
715 *Lett.* 429, 25-32, 2015.

716 Rustioni, G., Audetat, A. and Keppler, H.: Experimental evidence for fluid-induced melting in subduction
717 zones. *Geochem. Perspect. Lett.* 11, 49-54, 2019.

718 Sanchez-Valle, C.: Structure and thermodynamics of subduction zone fluids from spectroscopic studies.
719 *Rev. Mineral. Geochem.* 76, 265-309, 2013.

720 Sanchez-Valle, C., Martinez, I., Daniel, I., Philippot, P., Bohic, S., and Simionovici, A.: Dissolution of
721 strontianite at high P-T conditions: An in-situ synchrotron X-ray fluorescence study. *Am. Mineral.*
722 88, 978-985, 2003.

723 Sanchez-Valle, C., Daniel, I., Martinez, I., Simionovici, A., and Reynard, B.: Progress in quantitative
724 elemental analyses in high P-T fluids using synchrotron x-ray fluorescence (SXRF). *J. Phys.-*
725 *Condens. Mat.* 16, S1197-S1206, 2004.

726 Sandland, T. O., Du, L. S., Stebbins, F., and Webster, J. D.: Structure of Cl-containing silicate and
727 aluminosilicate glasses: A ³⁵Cl MAS-NMR study. *Geochim. Cosmochim. Ac.* 68, 5059-5069,
728 2004.

729 Schmidt, M.W., Vielzeuf, D. and Auzanneau E.: Melting and dissolution of subducting crust at high
730 pressures: the key role of white mica. *Earth Planet. Sc. Lett.* 228, 65-84, 2004.

731 Sherman, D.M.: Metal complexation and ion association in hydrothermal fluids: insights from quantum
732 chemistry and molecular dynamics. *Geofluids* 10, 41-57, 2010.

733 Signorelli, S. and Carroll, M. R.: Experimental study of Cl solubility in hydrous alkaline melts:
734 constraints on the theoretical maximum amount of Cl in trachytic and phonolitic melts. *Contrib.*
735 *Mineral. Petr.* 143, 209-218, 2002.

736 Silvestrelli, P. L. and Parrinello, M.: Structural, electronic, and bonding properties of liquid water from
737 first principles. *J. Chem. Phys.* 111, 3572-3580, 1999.

738 Skora, S. and Blundy, J.: High-pressure hydrous phase relations of radiolarian clay and implications for
739 the involvement of subducted sediment in arc magmatism. *J. Pet.* 51, 2211-2243, 2010.

740 Soper, A. K. and Benmore, C. J.: Quantum Differences between Heavy and Light Water. *Phys. Rev. Lett.*
741 101, 065502-1-4, 2008.

742 Stebbins, J. F. and Du, L. S.: Chloride ion sites in silicate and aluminosilicate glasses: A preliminary
743 study by Cl-35 solid-state NMR. *Am. Mineral.* 87, 359-363, 2002.

744 Stolper, E.: Water in silicate glasses: An infrared spectroscopic study. *Contrib. Mineral. Petr.* 81, 1-17,
745 1982.

746 Sverjensky, D.A., Harrison, B. and Azzolini, D.: Water in the deep Earth : The dielectric constant and the
747 solubilities of quartz and corundum to 60 kb and 1200 C. *Geochim. Cosmochim. Ac.* 129, 125-145,
748 2014.

749 Uchino, T., Sakka, T., Ogata, Y., and Iwasaki, M.: Mechanism of hydration of sodium-silicate glass in a
750 steam environment - Si²⁹ NMR and ab initio molecular-orbital studies. *Journal of Physical*
751 *Chemistry* 96, 7308-7315, 1992.

752 van Sijl, J., Allan, N. L., Davies, G. R., and van Westrenen, W.: Titanium in subduction zone fluids: First
753 insights from ab initio molecular metadynamics simulations. *Geochim. Cosmochim. Ac.* 74,
754 2797-2810, 2010.

755 Von Glasow, R., Bobrovski, N. and Kern, C.: The effects of volcanic eruptions on atmospheric chemistry.
756 *Chem. Geol.* 263, 131-142, 2009.

757 Wallace, P. J.: Volatiles in subduction zone magmas: concentrations and fluxes based on melt inclusion
758 and volcanic gas data. *J. Volcanol. Geoth. Res.* 140, 217-240, 2005.

759 Wallen, S. L., Palmer, B. J., Pfund, D. M., Fulton, J. L., Newville, M., Ma, Y. J., and Stern, E. A.:
760 Hydration of bromide ion in supercritical water: An X-ray absorption fine structure and molecular
761 dynamics study. *J. Phys. Chem. A* 101, 9632-9640, 1997.

762 Wasik, A., Dingwell, D.B., Courtial, P. and Hess, K.: Viscosity and chemical diffusion of halogens in
763 silicate melts: implications for volcanic degassing. *Eos Trans. AGU* 86 (52) Fall Meet. Suppl.,
764 Abstract V21E-0667, 2005.

765 Webster, J. D.: Partitioning of F between H₂O and CO₂ fluids and topaz rhyolite melt - Implications for
766 mineralizing magmatic-hydrothermal fluids in F-rich granitic systems. *Contrib. Mineral. Petr.* 104,
767 424-438, 1990.

768 Webster, J. D.: Water Solubility and Chlorine Partitioning in Cl-Rich Granitic Systems - Effects of Melt
769 Composition at 2 kbar and 800 °C. *Geochim. Cosmochim. Ac.* 56, 679-687, 1992.

770 Webster, J.D., Baker, D.R. and Aiuppa, A.: Halogens in mafic and intermediate-silica content magmas. In
771 D.E. Harlov and L. Aranovich (eds.), *The Role of Halogens in Terrestrial and Extraterrestrial*
772 *Geochemical Processes*, Springer Geochemistry, 307-430, 2018.

773 Wohlers, A., Manning, C.E. and Thompson, A.B.: Experimental investigation of the solubility of albite
774 and jadeite in H₂O, with paragonite + quartz at 500 and 600 °C, and 1-2.25 GPa. *Geochim.*
775 *Cosmochim. Ac.* 75, 2924-2939, 2011.

776 Xue, X. Y. and Kanzaki, M.: Dissolution mechanisms of water in depolymerized silicate melts:
777 Constraints from H-1 and Si-29 NMR spectroscopy and ab initio calculations. *Geochim.*
778 *Cosmochim. Ac.* 68, 5027-5057, 2004.

779 Yamashita, S., Behrens, H., Schmidt, B. C., and Dupree, R.: Water speciation in sodium silicate glasses
780 based on NIR and NMR spectroscopy. *Chem. Geol.* 256, 231-241, 2008.

781

782

783

784

785

786

787 **List of Tables and Figure captions:**

788

789 **Table 1.** Synthesis conditions and chemical compositions of the Na₂Si₂O₅ (NS2) and haplogranite (Hpg)
790 glasses employed as starting materials in this study.

791

792 **Table 2:** Bromine fluid-melt partition coefficients at different P-T conditions. Calculated fluid and melt
793 compositions and densities are also reported.

794

795 **Table 3.** Structural parameters derived from Br K-edge EXAFS analysis for the reference aqueous
796 solutions and silicate glasses at ambient conditions.

797

798 **Table 4:** Br K-edge EXAFS analysis of experimental high P-T fluids with various compositions.

799

800

801 **Figure 1.** Microphotographs of the compression chamber of the HDAC showing the Haplogranite - H₂O
802 (A, B, C) and NS2 - H₂O (D, E, F) systems at the indicated pressure and temperature conditions. Images
803 are taken through the diamond along the X-ray path. A) Haplogranite glass and 3 wt% NaBr aqueous
804 solution at room conditions; B) globulus of hydrous silicate melt in equilibrium with the aqueous fluid; C)
805 supercritical liquid (single fluid phase); D) NS2 glass and 3 wt% NaBr aqueous solution at room
806 conditions; E) supercritical liquid (low temperature supercriticality); F) hydrous NS2 melt coexisting with
807 aqueous fluid (high temperature subcriticality).

808

809 **Figure 2.** 2D-SXRF Br K_α intensity maps of Run 1 showing the distribution of Br between coexisting
810 aqueous fluid and haplogranite melt at different P-T conditions. The fluid:glass ratio refers to the wt

811 fraction calculated from the volumetric proportions of loaded glass and sample chamber. The white
812 dashed line delimits the edge of the Re gasket.

813 Br-enriched phases appear in red and yellow, Br-depleted areas in blue and green. At the beginning of the
814 experiment (A), all the Br is concentrated in the glass. After the glass melts (B), Br strongly partitions
815 into the fluid phase ($D_{Br}^{f/m} = 8.07 \pm 0.79$). As temperature increases, the Br concentration in the melt
816 increases while the Br concentrations in the fluid decreases (C). At 821°C - 0.9GPa, the I_f/I_m ratio appears
817 homogeneous as the Br concentrations per volume are almost similar ($I_f/I_m = 1.3 \pm 0.1$). However, per
818 weight, Br still partitions preferentially into the fluid ($D_{Br}^{f/m} = 2.02 \pm 0.14$).

819
820 **Figure 3. Evolution of the Br partition coefficients $D_{Br}^{f/m}$ with (A) increasing temperature at**
821 **different pressure conditions and (B) density ratio of coexisting fluids and melts for given P - T .** The
822 different symbols and colors account for separate experimental runs involving different glass proportions.
823 **The errors reported on $D_{Br}^{f/m}$ take into account analytical uncertainties on the SXRF signal**
824 **intensities in fluid and melt and an additional uncertainty of 10% on pressure determination. The**
825 **Br and Cl fluid/melt partition coefficients from Bureau et al. (2000, 2010), Cadoux et al. (2018) and**
826 **Webster (1992) are shown for comparison.** For Cadoux et al., note that both average values from
827 several experiments ($D_{Br}^{f/m} = 20.2 \pm 1.2$) and minimum value for a single experiment ($D_{Br}^{f/m} = 8.6$) are
828 reported. **For Webster (1992), the solid and dotted symbols are for experiments where Cl in glass was**
829 **< 0.01 wt% and 0.01-0.03 wt%, respectively.**

830
831 **Figure 4.** Normalized Br K-edge XANES spectra collected on Br-bearing silicate glasses, aqueous fluids
832 and hydrous silicate melts at various pressure and temperature conditions. Spectra are offset for clarity.
833 The vertical dashed line is a visual guide to appreciate phase shifts. The black arrow shows the pre-edge

834 feature in the haplogranite glass spectrum corresponding to the 1s to 4p transition in Br (Burattini et al.,
835 1991).

836

837 **Figure 5.** Normalized k^1 -weighted EXAFS oscillations of the investigated Br-bearing samples (black
838 solid lines) and corresponding least-square fits (blue dashed lines). Spectra are off-set vertically for
839 clarity. The pressure and temperature conditions and the compositions are reported right to each spectrum.
840 The dashed lines underline the shift of EXAFS oscillations with change in composition.

841

842 **Figure 6.** Evolution of bromine coordination numbers with oxygen (from H₂O molecules) and sodium
843 ($N_{\text{Br}\cdots\text{H-O}}$ and $N_{\text{Br-Na}}$) as a function of fluid composition (*i.e.*, the weight fraction of NS2 dissolved in the
844 fluid) along the NaBr aqueous solution – NS2 join. The gray field shows the detection limit (DL) for Br-
845 Na complexes, which corresponds to the maximum Br-Na coordination number ($N_{\text{Br-Na}}$) determined for
846 3wt% NaBr aqueous solution at ambient conditions and 450 °C (DL < 1.5 atoms).

847

848 **Table 1.**

Sample	Synthesis conditions		Br ¹ (wt%)	Na ₂ O ² (wt%)	SiO ₂ ² (wt%)	Al ₂ O ₃ ² (wt%)	K ₂ O ² (wt%)	H ₂ O ³ (wt%)	ASI ⁴	Analytical method
	T (°C)	P(GPa)								
NS2- Br1	1200	0.5	4.01 4.10	32.0	63.9					EMPA LA-ICPMS
Hpg- Br2	1200	1.5	- 0.96	7.1	74.1	9.2	3.7	3.3	0.57	EMPA RBS
Hpg- Br3	1200	1.5	0.89	7.4	75.0	9.4	3.8	3.3	0.57	EMPA

849
850
851
852
853
854
855
856
857
858
859
860
861
862
863
864
865
866
867
868
869
870
871
872
873
874
875
876
877

Notes: EMPA = Electron Microprobe Analyses; LA-ICPMS = Laser-ablation Inductively Couple Plasma Mass Spectrometry; RBS = Rutherford Backscattering Spectroscopy.

¹Standard deviations (1σ) are 0.04 wt% for RBS analysis, 0.3 wt% for LA-ICPMS and 0.03 wt% for EMPA analysis.

²Average from 10 to 25 analyses performed on each glass composition. Standard deviations (1σ) are < 0.1 wt% for Na₂O, Al₂O₃ and K₂O and < 0.3 wt% for SiO₂.

³Nominal H₂O concentration (not analyzed).

⁴Aluminum Saturation Index $ASI = \frac{Al_2O_3}{Na_2O+K_2O}$ (in moles).

878

879 **Table 2.**

X_g^1	T (°C)	P (GPa) ²	H ₂ O in melt (wt%) ³	Melt density ρ_m^4	Transmission in melt T _m	Silicates in fluid (wt%) ⁵	Fluid density ρ_f^7	Transmission in fluid T _f	I_{Br}^f/I_{Br}^m	$D_{Br}^{f/m}$
Haplogranite – H₂O										
<i>Run 1</i>										
0.76	592	0.7	7.1 ±0.8	2.24	0.66	2.5 ±0.5	0.94	0.96	4.9	8.1 ±1.6
	694	0.8	7.7 ±0.9	2.23	0.67	5.3 ±1.2	0.97	0.95	2.6	4.2 ±0.4
	821	0.9	8.0 ±1.0	2.23	0.67	10.3 ±2.3	0.99	0.95	1.3	2.0 ±0.2
<i>Run 2</i>										
0.82	645	0.9	9.1 ±1.1	2.22	0.67	5.5 ±1.1	1.02	0.95	10.0	15.3 ±2.0
	710	1.1	11.1 ±1.4	2.20	0.68	11.1 ±2.4	1.09	0.94	5.4	7.9 ±1.0
	840	0.9	7.9 ±1.0	2.23	0.67	10.8 ±2.4	0.98	0.95	2.8	4.4 ±0.6
<i>Run 3</i>										
0.72	610	1.2	13.3 ±1.7	2.18	0.69	7.7 ±1.6	1.13	0.95	4.6	6.4 ±0.6
	730	0.65	6.0 ±0.7	2.25	0.66	3.9 ±0.9	0.88	0.96	2.3	4.1 ±0.8
	800	0.2	2.4 ±0.2	2.26	0.64	0.7 <0.1	0.49	0.98	1.6	4.8 ±0.6
Haplogranite – 3 wt% NaBr aqueous solution										
<i>Run 4</i>										
0.70	740	1.7	19.5 ±2.8	2.11 ±0.02	0.72	12.8 ±0.8 ⁶	1.20	0.94	7.2	9.7 ±1.2
<i>Error (unless indicated)</i>		±0.1		±0.01	±0.07		±0.04	±0.01	±0.04-0.43	

880

881

Notes:

882

¹ Initial weight fraction of glass in the loading.

883

² Maximum **estimated** uncertainty on pressure **for the calculations** were of 10%.

884

³ H₂O solubility in the haplogranite melt calculated from the solubility data of Mysen and Wheeler (2000).

885

⁴ Melt density (in g.cm⁻³) calculated as a function of P-T conditions and melt composition using Malfait et al. (2014).

886

⁵ Solubility of silicate components (SiO₂, Na₂O, Al₂O₃ and K₂O) in the aqueous fluid coexisting with haplogranite melt calculated from the albite solubility data of Anderson and Burnham (1983).

887

888

⁶ Silicate solubility in the aqueous fluid estimated from Wohlers et al. (2011) for P > 1.2 GPa.

889

⁷ Fluid density (in g.cm⁻³) calculated as a function of P-T conditions from the data of Mantegazzi et al. (2013)

891

892 **Table 3.**

Composition	Oxygen (O)			Sodium (Na)			
<i>Aqueous solutions</i> ¹							
	$N_{\text{Br}\cdots\text{H-O}}$	$R_{\text{Br}\cdots\text{H-O}} (\text{Å})$	$\sigma^2 (\text{Å}^2)$				<i>R-factor</i>
3 wt% NaBr-H₂O	5.9 ±0.7	3.37 ±0.04	0.02				0.04
2.3 wt% KBr-H₂O ³	5.7 ±0.8	3.30 ±0.03	0.02				0.06
<i>Silicate glasses</i> ²							
	$N_{\text{Br-O}}$	$R_{\text{Br-O}} (\text{Å})$	$\sigma^2 (\text{Å}^2)$	$N_{\text{Br-Na}}$	$R_{\text{Br-Na}} (\text{Å})$	$\sigma^2 (\text{Å}^2)$	<i>R-factor</i>
NS2 glass	5.2 ±2.4	3.45 ±0.09	0.02	5.3 ±1.8	2.99 ±0.09	0.03	0.25
Haplogranite glass	6.1 ±3.6	3.39 ±0.03	0.02	5.9 ±1.8	2.94 ±0.03	0.03	0.21

893

894 **Notes:** N = Br coordination number ($N_{\text{Br-O}}$ or $N_{\text{Br-Na}}$); R = Br-neighbor (Na or O) mean distance (Å); σ^2 = squared Debye-Waller
 895 factor (Å²); *R-factor* = goodness of the fit; $S_0^2 = 1$;

896 ¹ Hydration shell (Br⁺·H-O)

897 ² Br coordinated to oxygens from the silicate network (next-nearest coordination shell).

898 ³ Ferlat et al. (2002), 0.2m KBr-H₂O for comparison.

899

900 **Table 4.**

Composition	T (°C)	P (GPa)	N _{Br...H-O}	R _{Br...H-O} (Å)	σ ² (Å ²)	N _{Br-Na}	R _{Br-Na} (Å)	σ ² (Å ²)	R-factor
<i>3 wt% NaBr aqueous solution</i>									
	25	0	5.9 ± 0.7	3.37 ± 0.04	0.02	bdl ¹			0.04
	320	0.2	6.3 ± 1.8	3.36 ± 0.05	0.04	bdl			0.17
	450	0.6	6.4 ± 1.1	3.40 ± 0.07	0.05	bdl			0.19
<i>Br-bearing aqueous fluids</i>									
1.2 wt% Hpg³	475	1	5.4 ± 0.9	3.33 ± 0.03	0.05	bdl			0.13
5 wt% Hpg	680	0.8	5.7 ± 1.1	3.30 ± 0.04	0.06	bdl			0.12
0.6 wt% Hpg	750	0.2	5.0 ± 1.6	3.33 ± 0.06	0.06	bdl			0.30
30 wt% NS2²	190	n.d.	6.7 ± 1.4	3.38 ± 0.03	0.04	bdl			0.14
	320	n.d.	5.7 ± 1.4	3.37 ± 0.09	0.04	bdl			0.22
50 wt% NS2	580	1.1	4.7 ± 1.5	3.35 ± 0.15	0.04	bdl			0.25
<i>Br-bearing melt-like fluids</i>									
60 wt% NS2	480	1.5	3.6 ± 1.5	3.47 ± 0.05	0.01	2.5 ± 1.2	3.10 ± 0.06	0.01	0.23
	610	2.2	4.8 ± 2.4	3.45 ± 0.05	0.03	2.6 ± 0.9	3.06 ± 0.06	0.03	0.20
NS2 melt (10 ± 1 wt% H₂O)	710	0.4	3.4 ± 1.6	3.36 ± 0.03	0.02	6.6 ± 2.1	2.91 ± 0.03	0.05	0.24

901 **Notes:** N = Br coordination number (dissociate as N_{Br...H-O} and N_{Br-Na}); R = Br-neighbor mean distance (Å); σ² = squared Debye-
902 Waller factor (Å²); R-factor = goodness of the fit; S₀² = 1.

903 ¹bdl = below detection limit. Detection limit corresponds to the maximum Br-Na coordination number determined for 3 wt%
904 NaBr aqueous solution at ambient conditions.

905 ²wt% NS2 indicates the amount of dissolved NS2 in the single phase fluid calculated from the mass of H₂O and NS2 glass.

906 ³wt% Hpg refers to the amount of dissolved silicate in the fluid coexisting with haplogranite melt calculated as in Table 2.

907 Errors in temperature and pressure are ±2 °C and 10%, respectively. Errors in the composition of the analyzed fluids are within
908 5% (Table 2).

909

910

911

912

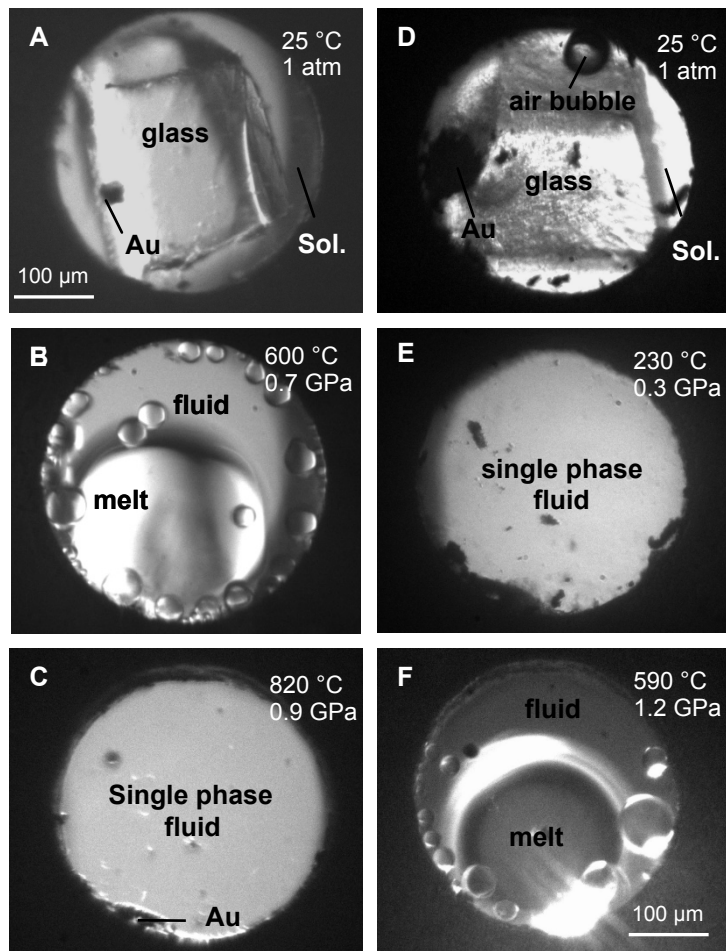
913

914

915

916

917



919

920

921 **Figure 1**

922

923

924

925

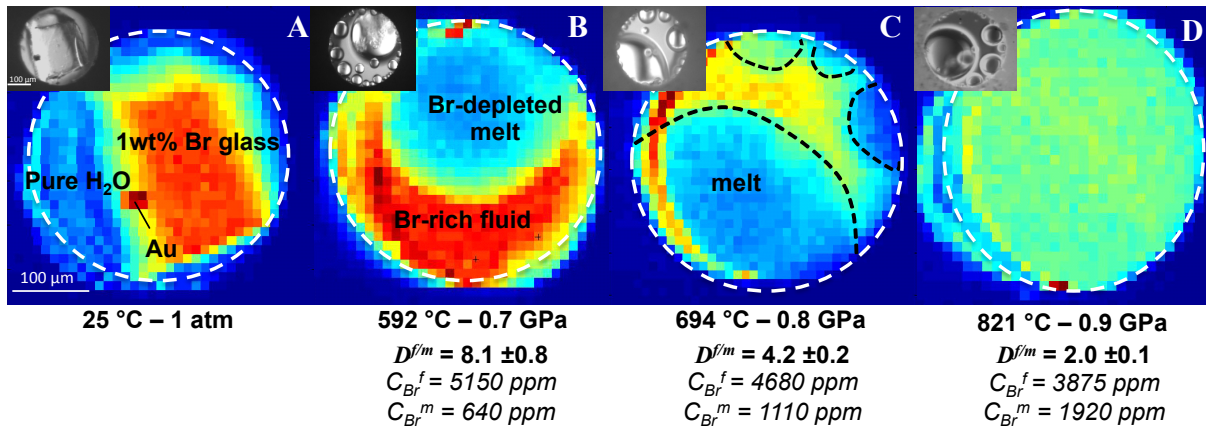
926

927

928

929

Run 1 – Fluid:Glass ratio = 0.76



930

931 **Figure 2**

932

933

934

935

936

937

938

939

940

941

942

943

944

945

946

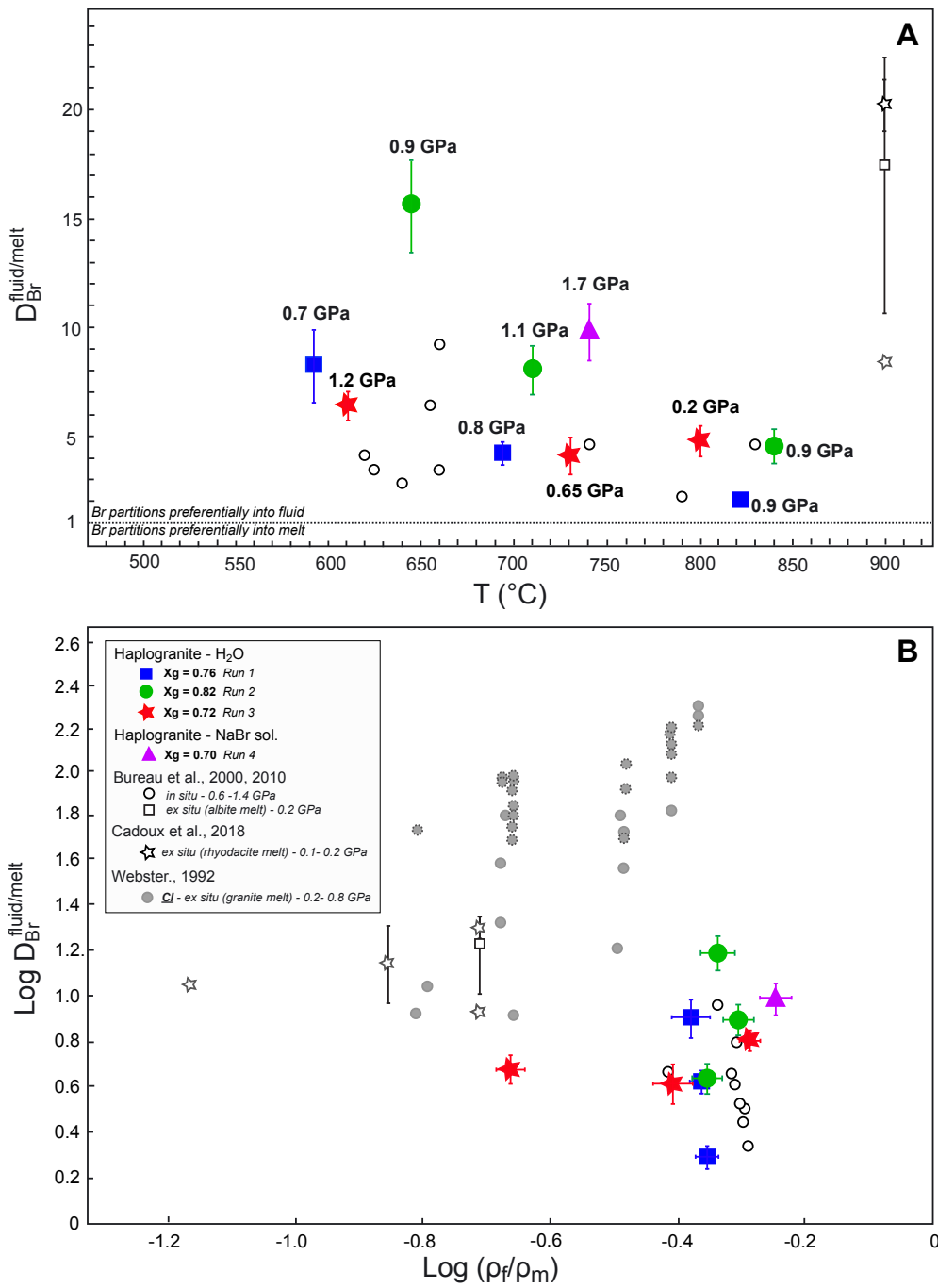
947

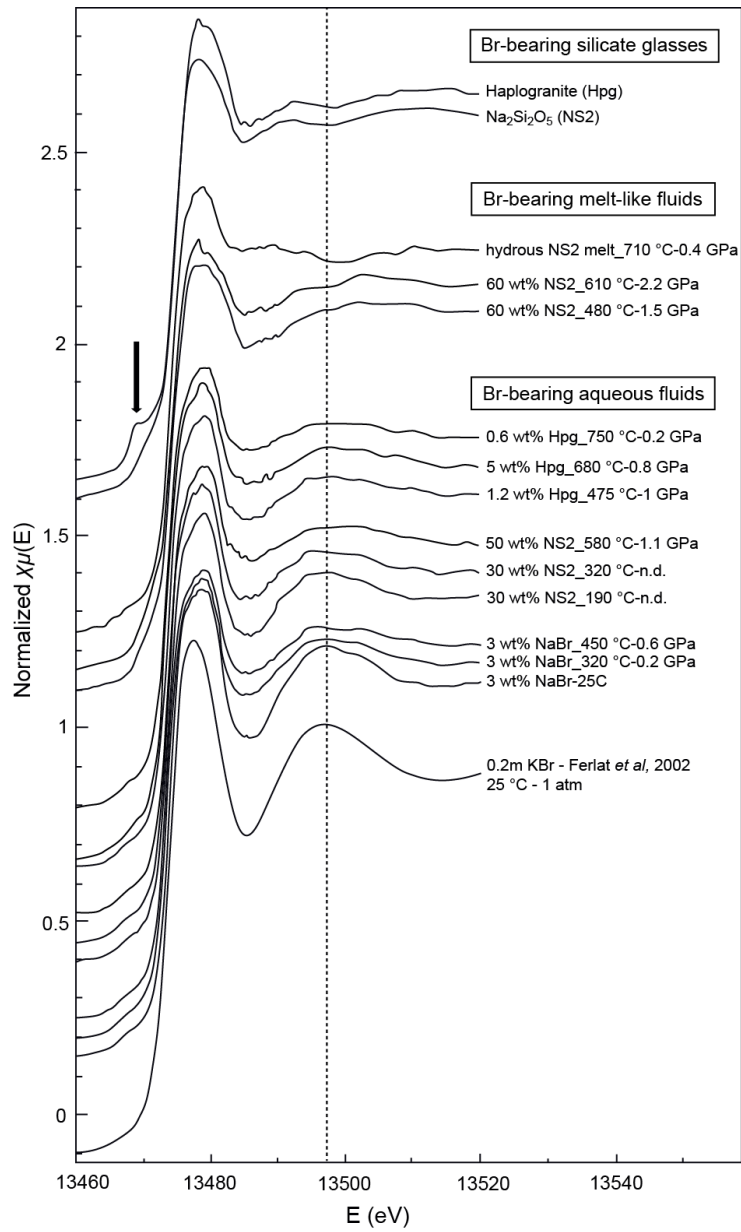
948

949

950

951





957

958 **Figure 4**

959

960

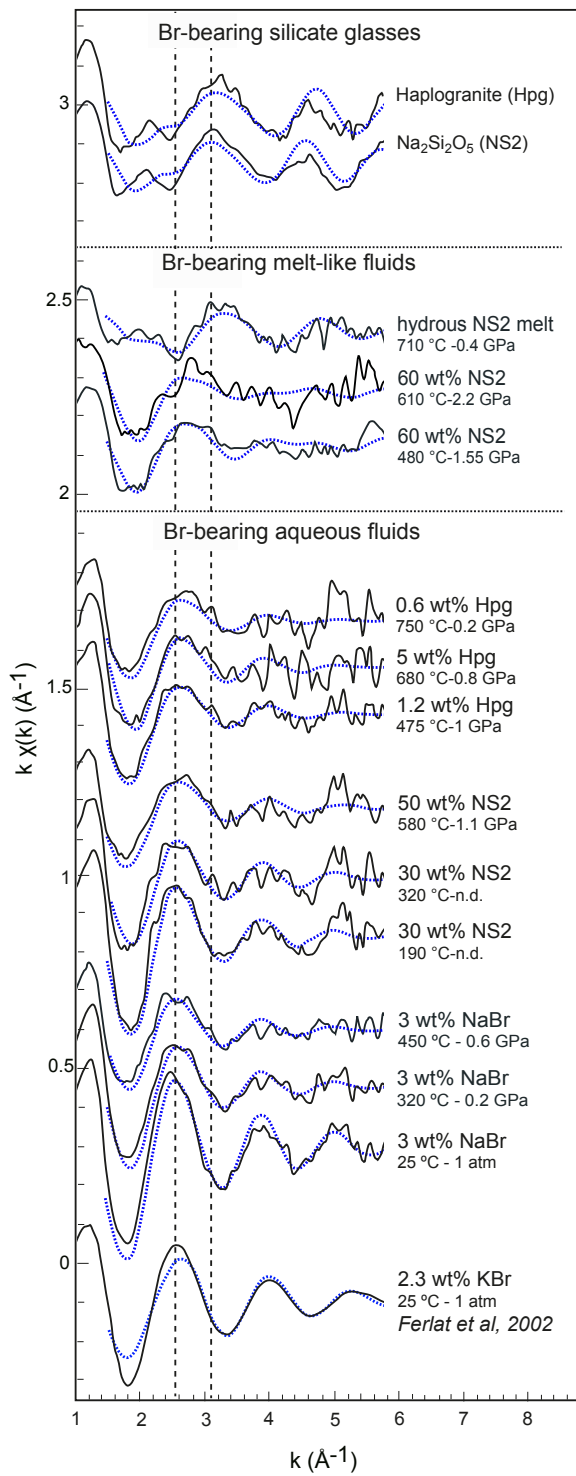
961

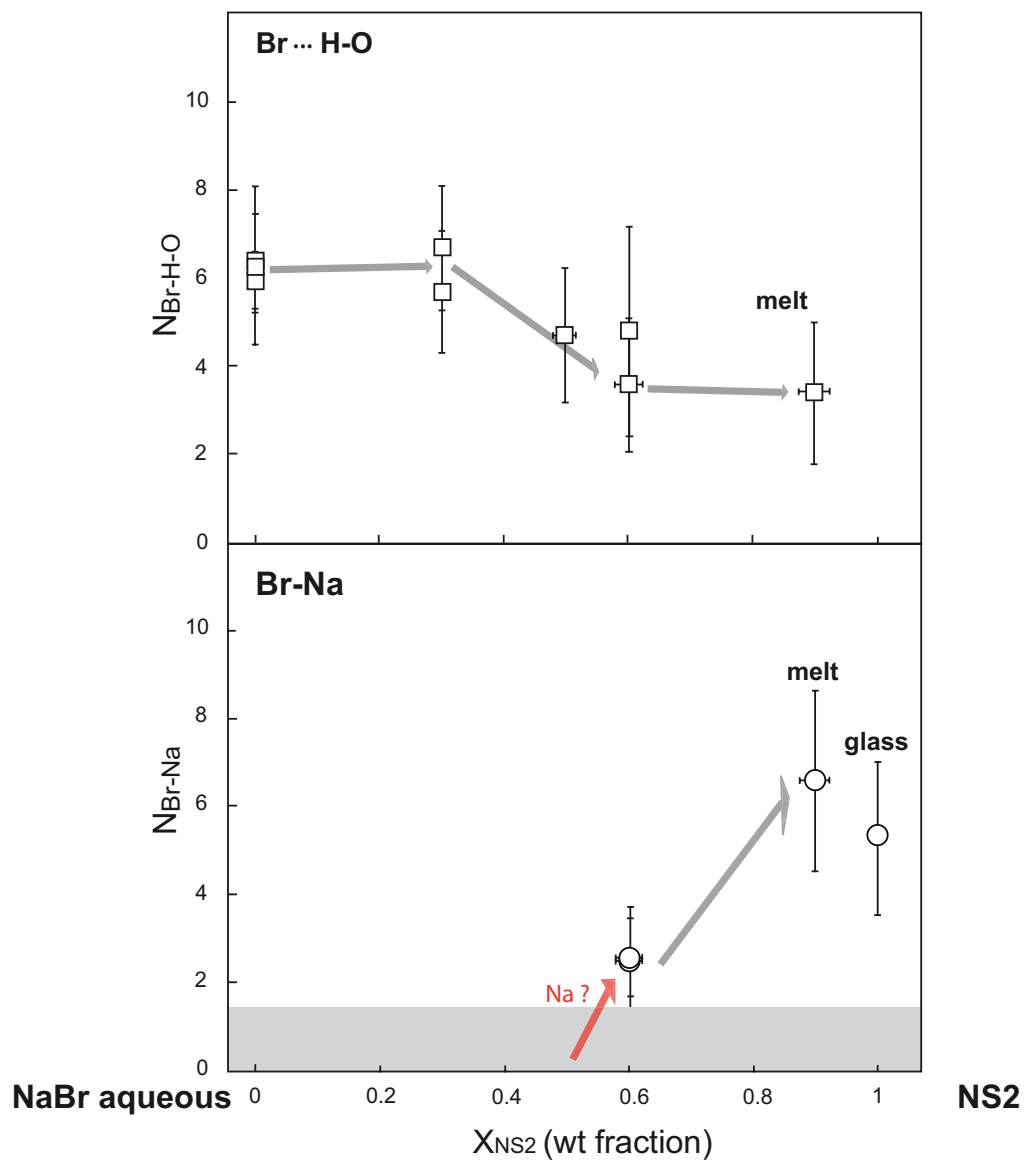
962

963

964

965





970

971

972 **Figure 6**